Chromosome Structure II: Stem-loops and circle-loops.

Wenfan Ke[1]*, Miki Fujioka[2]*, Paul Schedl[1], and James B. Jaynes[2]

1: Department of Molecular Biology, Princeton University, Princeton NJ 08544

2: Department of Biochemistry and Molecular Biology, Thomas Jefferson University, Philadelphia, PA 19107

* These authors contributed equally.

Abstract

The chromosomes in multicellular eukaryotes are organized into a series of topologically independent loops called TADs. In flies, TADs are formed by physical interactions between neighboring boundaries. Fly boundaries exhibit distinct partner preferences, and pairing interactions between boundaries are typically orientation dependent. Pairing can be head-to-tail or head-to-head. The former generates a stem-loop TAD, while the latter gives a circle-loop TAD. The TAD that encompasses the *Drosophila even skipped* (*eve*) gene is formed by the head-to-tail pairing of the *nhomie* and *homie* boundaries. To explore the relationship between loop topology and the physical and regulatory landscape, we flanked the *nhomie* boundary region with two attP sites. The attP sites were then used to generate four boundary replacements: *λ DNA*, *nhomie forward* (WT orientation), *nhomie reverse* (opposite of WT), and *homie forward* (same as WT *homie*). The *nhomie forward* replacement restores the WT physical and regulatory landscape: In MicroC experiments, the *eve* TAD is a volcano triangle topped by a plume, and the *eve* gene and its regulatory elements are sequestered from interactions with neighbors. The *λ DNA* replacement lacks boundary function: the endpoint of the "new" *eve* TAD on the *nhomie* side is ill-defined, and *eve* stripe enhancers activate a nearby gene, *eIF3j*. While *nhomie reverse* and *homie forward* restore the *eve* TAD, the topology is a circle-loop, and this changes the local physical and regulatory landscape. In MicroC experiments, the *eve* TAD interacts with its neighbors, and the plume at the top of the *eve* volcano triangle is replaced by a cloud of contacts with the next-door TADs. Consistent with the loss of isolation afforded by the stem-loop topology, the *eve* enhancers weakly activate genes in the neighboring TADs. Conversely, *eve* function is partially disrupted.

Introduction

Chromosomes in multicellular animals are organized into a series of topologically independent looped domains, called TADs (topologically associated domains: (Cavalheiro et al., 2021; Chetverina et al., 2017; Jerković et al., 2020; Matthews and White, 2019; Rowley and Corces, 2018). The arrangement of TADs in a given chromosomal DNA segment is generally (though not precisely) similar in different tissues and developmental stages, and this is a reflection of the mechanism underlying TAD formation—the endpoints of TADs are determined by a special class of elements called chromatin boundaries or insulators. While boundary-like elements have been identified in a wide range of animals and plants, the properties of this class of DNA elements have been most fully characterized in *Drosophila* (Cavalheiro *et al.*, 2021; Chetverina *et al.*, 2017). Fly boundaries have one or more large (100-400 bp) nucleosome-free nuclease hypersensitive sequences that are targets for multiple DNA binding chromosomal architectural proteins. While only a single chromosomal architectural protein, CTCF, has been characterized in mammals, there are almost two dozen such proteins in flies and the list is still growing (Heger et al., 2013; Heger and Wiehe, 2014; Schoborg and Labrador, 2010). In addition to subdividing the chromosome into a series of loops, fly boundary elements have insulating activity. When placed between enhancers or silencers and their target promoters, boundaries block regulatory interactions (Bell et al., 2001; Chetverina et al., 2014; Chetverina *et al.*, 2017). This activity provides a mechanism for delimiting units of independent gene activity: genes located between a pair of compatible boundaries are subject to regulatory interactions with enhancers/silencers present in the same chromosomal interval, while they are insulated from the effects of enhancers/silencers located beyond either boundary in adjacent regulatory neighborhoods. It is currently thought that their ability to organize the chromosome into

62 topologically independent loops is important for their insulating activity (Cai and Shen, 2001;
63 Gohl et al., 2011; Muravyova et al., 2001).

64 Studies dating back to the '90's have suggested that fly boundaries subdivide the
65 chromosome into loops by physically pairing with each other (Chetverina *et al.*, 2014;
66 Chetverina *et al.*, 2017). In these first experiments, regulatory interactions were observed for
67 transgenes inserted at distant sites in chromosome that were carrying either the *gypsy* transposon
68 boundary *su(Hw)* or the bithorax complex (BX-C) boundary *Mcp* (Muller et al., 1999; Sigrist and
69 Pirrotta, 1997; Vazquez et al., 1993). Further support for the idea that boundaries function by
70 pairing has come from chromatin immunoprecipitation, chromosome conformation capture
71 (CCC), MicroC, and direct imaging experiments (Chen et al., 2018; Li et al., 2011; Vazquez et
72 al., 2006). More recent studies have revealed physical interactions in the CNS, such as those
73 found for *su(Hw)* and *Mcp,* which "reach over" multiple intervening TADs, consistent with them
74 playing an important role in cell type-specific gene regulation (Mohana et al., 2023) by bringing
75 distant enhancers and promoters together.

76 The parameters governing pairing interactions have been defined using insulator bypass,
77 transvection and boundary competition assays. These studies have shown that fly boundaries are
78 able to pair not only with heterologous boundaries but also with themselves. Moreover, the
79 pairing interactions typically exhibit a number of characteristic features: promiscuity coupled
80 with clear partner preferences, and orientation dependence.

81 Partner preferences depend upon the chromosomal architectural proteins that interact
82 with each boundary. For example, in the boundary bypass assay, a set of enhancers are placed
83 upstream of two reporters (Cai and Shen, 2001; Kyrchanova et al., 2008a; Muravyova *et al.*,
84 2001). When multimerized CTCF sites are placed between the enhancers and the closest
85 reporters, both reporters are insulated from the enhancers. When a second set of multimerized

86 CTCF sites are place downstream of the closest reporter, bypass is observed. In this case the
87 closest reporter, which is bracketed by the multimerized CTCF sites, is still insulated from the
88 enhancers; however, the downstream reporter is activated (Muravyova *et al.*, 2001).
89 Heterologous combinations give a different result: when multimerized dCTCF sites are placed
90 upstream of the closest reporter and multimerized Zw5 sites are placed downstream, no bypass is
91 observed. Endogenous fly boundaries also show partner preferences in bypass assays and in
92 boundary competition experiments (Gohl *et al.*, 2011; Kyrchanova et al., 2011; Kyrchanova et
93 al., 2008b). On the other hand, while boundaries have partner preferences, they are also
94 promiscuous in their ability to establish functional interactions with other boundaries. For
95 example, the *Fab-8* insulator can pair with *scs'* from the *Drosophila* heat shock locus (Gohl *et*
96 *al.*, 2011).
97 In addition, to partner preferences, pairing interactions between endogenous fly
98 boundaries are, with a few exceptions, orientation dependent. Self-pairing interactions are head-
99 to-head. This seems to be a common feature of fly boundaries and has been observed for *scs*,
100 *scs'*, *iA2*, *wari*, *Mcp*, *Fab-8*, *AB-I, homie* and *nhomie* (Fujioka et al., 2016; Kyrchanova *et al.*,
101 2008a). In contrast, pairing interactions between heterologous boundaries can be head-to-head
102 or head to tail. The two boundaries bracketing the *even-skipped* (*eve*) locus, *homie* and *nhomie*,
103 pair with each other head-to-tail, while boundaries in the *Abdominal-B* (*Abd-B*) region of BX-C
104 pair with their neighbors head-to-head. The topology of the loops (TADs) generated by head-to-
105 tail and head-to-head pairing between neighboring boundaries in *cis* are different. As illustrated
106 in Fig. 1, head-to-tail pairing generates stem-loops, while head-to-head pairing generates circle-
107 loops. The loops could be connected to each other by unanchored loops (Fig. 1A and C), or they
108 could be linked directly to each other if boundaries can pair simultaneously with both neighbors
109 (Fig 1B and D). An alternating pattern of TADs connected by DNA segments that crosslink to

110 each other with reduced frequency (c.f., λ DNA below) is not observed in MicroC experiments.
111 Instead, most TADs appeared to be directly connected to both of their neighbors without an
112 intervening unanchored loop (Batut et al., 2022; Bing et al., 2023; Levo et al., 2022): see also
113 below). This would suggest that TAD boundaries are typically linked to both neighbors, either
114 simultaneously or as alternating pair-wise interactions.

115 Key to understanding the 3D organization of chromosomes in multicellular eukaryotes
116 will be the identification of TADs that are stem-loops and TADs that are circle-loops. In the
117 studies reported here, we have used MicroC to analyze the contact maps generated by stem-loops
118 and circle-loops. Stem-loops and circle-loops TADs are expected to interact differently with
119 their neighbors and this should be reflected in the patterns of crosslinking events between
120 neighboring TADs. As illustrated for linked stem-loops in Fig. 1B, TAD2, is isolated from its
121 next-door neighbors, TAD1 and TAD3. In this configuration, crosslinking events between
122 sequences in TAD2 and sequences in TAD1 and TAD3 will be suppressed. On the other hand,
123 TAD1 and TAD3 are in comparatively close proximity, and crosslinking between sequences in
124 these two TADs will be enhanced. A different pattern of neighborly interactions is expected for
125 circle-loop TADs. In this case, the TAD in the middle, TAD2, is expected to interact with both
126 of its neighbors (Fig. 1D). To test these predictions, we have first compared the MicroC contact
127 profiles for stem-loop and circle-loop TADs. For stem-loops we selected the *eve* TAD, while for
128 circle-loops we chose the four TADs that comprise the *Abd-B* parasegment-specific regulatory
129 domains. We show that these stem-loop and circle-loop TADs have distinctive crosslinking
130 signatures. To confirm these MicroC signatures we converted the topology of the *eve* TAD from
131 a stem-loop to a circle-loop. In addition to changing the MicroC signature of the *eve* TAD, the
132 change in topology is accompanied by changes in the regulatory interactions between *eve* and its
133 neighbors.

134 **Results**

135 ***Stem-loops versus circle-loops***

136 The distinctive loop topologies of stem-loops and circle-loops are expected to be reflected in
137 the contact maps that are generated in MicroC experiments. To determine if this is the case, we
138 compared the MicroC contact maps for the *eve* TAD and the TADs that correspond to the four
139 *Abd-B* parasegment specific regulatory domains, *iab-5*, *iab-6*, *iab-7* and *iab-8*. The *eve* TAD is
140 generated by pairing interactions between the *nhomie* boundary upstream of the *eve* transcription
141 unit and the *homie* boundary downstream. Since *nhomie* and *homie* pair with each other head-to-
142 tail, the *eve* TAD has a stem-loop topology. Unlike the *eve* boundaries, the boundaries that
143 delimit the *Abd-B* regulatory domains are thought to pair with their neighbors head-to-head
144 (Chetverina *et al.*, 2017; Kyrchanova *et al.*, 2008a; Kyrchanova *et al.*, 2011; Kyrchanova *et al.*,
145 2008b)). This means that the parasegment-specific regulatory domain TADs, *iab-5*, *iab-6*, *iab-7*
146 and *iab-8*, are expected to have a circle-loop topology.

147 As shown in Fig. 2, the *eve* TAD and the four *Abd-B* TADs have distinctive MicroC contact
148 patterns. The *eve* TAD is a volcano triangle with a plume. The endpoints of the volcano triangle
149 are delimited by *nhomie* on the left and *homie* on the right, and within the *eve* locus (the
150 volcano), there are additional enhanced interactions. While the volcano triangle is generated by
151 contacts between sequences within the *eve* stem-loop, contacts between sequences in *eve* and in
152 the neighboring TAD on the left, TL (which contains multiple sub-TADs and six genes:
153 *CG15863, CG1418*, *Pal1, CG12133, eIF3j* and *CG12134*), are much reduced (L-ev in Fig 2A).
154 There is a similar suppression of contacts between sequences in the *eve* TAD and sequences in
155 the large neighboring TAD on the right, TM (which contains *TER94* and *Pka-R2*) (ev-M in Fig
156 2A). On the other hand, as expected from the regulatory interactions observed for stem-loops in
157 boundary bypass experiments (Kyrchanova *et al.*, 2008a), physical contacts between sequences

158 in TL and TM are enhanced compared to those between *eve* and TL (L-ev) or TM (ev-M).
159 Because of the preferential interactions between TADs to either side of the *eve* stem-loop, the
160 *eve* volcano triangle is topped by a plume (L-M in Fig. 2A). TM also interacts with the two of
161 TADs farther to the left of *eve*, TK (K-M in Fig. 2A) and TJ (J-M in Fig. 2A) (see also Fig.
162 Supplemental 1).

163 Like the *eve* boundaries, the TADs in the *Abd-B* region of BX-C region are connected to
164 their neighbors by the boundaries at their base. As predicted from genetic studies on BX-C
165 boundaries, each TAD corresponds to one of the four parasegment-specific regulatory domains.
166 While the MicroC contact maps for the four *Abd-B* TADs resemble the contact patterns in the
167 *eve* TAD, these *Abd-B* TADs differ from *eve* in that there are no plumes at the top of their
168 volcano triangle (Fig. 2B). Instead, the *Abd-B* TADs are overlaid by a series of rectangular
169 interlocking low-density contact (LDC) domains, or clouds. As illustrated in Fig 2B, the *iab-6*
170 regulatory domain is surrounded by clouds generated by crosslinking with its next door
171 neighbors *iab-5* (5-6) and *iab-7*(6-7), followed by crosslinking with neighbors that are a TAD
172 away from *iab-6*, *iab-4* (4-6) and *iab-8* (6-8). The other regulatory domains also form a unique
173 set of interlocking LDCs/clouds with their immediate neighbors, their next-next door neighbors,
174 and their next-next-next door neighbors.

175 ***TAD formation in a nhomie deletion***

176 To further investigate the pairing properties and functioning of the *eve* boundaries, we used
177 CRISPR-Cas9 to add two attP sites flanking the *nhomie* region, replacing the region with a mini-
178 *white* gene. Using mini-*white* as an exchange maker, ΦC31 recombinase-mediated cassette
179 exchange (RMCE) was used to restore the sequence of the region, with *nhomie* modifications.
180 As a control for possible effects of the sequences introduced in generating the modification, we
181 reinserted a 597 bp *nhomie* DNA fragment in the same orientation as the endogenous *nhomie*

182 boundary (*nhomie forward*). To maintain roughly the same distance between *eve* and the
183 neighboring TAD in the *nhomie* deletion, we introduced a 606 bp DNA fragment from phage
184 λ (*λ DNA*). Fig. 3 (and Fig. Supplemental 1) shows the MicroC contact profiles for the *nhomie*
185 *forward* and *λ DNA* replacements. Except that the sequencing depth of the *nhomie forward*
186 replacement is not as great as the WT shown for the *eve* locus in Fig. 2, the profile is quite
187 similar. Like WT, there are sub-TADs within the *eve* TAD. One of these appears to link *homie*
188 and the neighboring PRE to the *eve* promoter-proximal PRE (Fujioka et al., 2008), and is marked
189 by an interaction dot (asterisk in Fig. 3A). Another links *nhomie* to the *eve* promoter region
190 (blue arrow in Fig. 3A). The *eve* TAD is topped by a plume which is generated by interactions
191 between sequences in neighboring TADs TL with TM (L-M). On the other hand, interactions
192 between *eve* and its neighbors are suppressed. Like *eve*, there are sub-TADs in the neighboring
193 TAD, TL. The TL sub-TAD closest to *eve* (TL4) corresponds to the *CG12134* transcription unit
194 (green arrowhead marks the boundary: Fig. 3), while the neighboring sub-TAD (TL3)
195 encompasses the *eIF3j* transcription unit (blue arrowhead: Fig. 3).

196 The MicroC profile of the *λ* DNA replacement (Fig. 3D) is quite different from that of
197 either *nhomie forward* or WT, which are similar (Figs. 2A and 3A). While *homie* still defines
198 the distal (relative to the centromere) end of the *eve* locus, the *λ DNA* replacement does not
199 function as a TAD boundary, and the leftward endpoint of the *eve* TAD is no longer well-
200 defined. One new "endpoint" for the *eve* locus maps to sequences between *CG12134* and *eIF3j*
201 (green arrowhead), which in wild type correspond to the left boundary of the TL sub-TAD TL4.
202 The other endpoint maps to sequences between *eIF3j* and *CG12133* (blue arrowhead), which in
203 wild type define the left boundary of the TL sub-TAD TL3. These interactions are not as stable
204 as those between *nhomie* and *homie*, as the density of interaction dots is lower. Furthermore,
205 they appear to flip back and forth between alternative endpoints (as indicated by the green and

206 blue double arrows in Fig. 3F) based on the MicroC contact profile, which is consistent with a
207 mixture of (at least) two conformations. The *eve* TAD also interacts with sequences in the two
208 other TL sub-TADs, TL1 and TL2. In addition, the *eve* promoter appears to interact with
209 sequences located upstream of *CG12134* (purple arrowhead in Fig. 3D and double arrow in Fig.
210 3F), while this interaction is not observed in the *nhomie forward* replacement. While the TL
211 TAD (from the TK:TL boundary to *nhomie*) is also disrupted by the *nhomie* deletion (it has a
212 much less distinct "volcano apex", and its right-most sub-TAD TL4 is now fused with the *eve*
213 TAD), the left-most TL sub-TADs (TL1, TL2, and TL3) are still present, indicating that their
214 formation does not depend on *nhomie*. As shown in the virtual 4C at *homie* viewpoint in Fig. 3B
215 and Fig. 3E, the *homie* boundary interacts with the *nhomie forward* replacement, but does not
216 contact the *λ DNA* replacement.

217 ***eve* enhancers activate *eIF3j* expression in the *nhomie* deletion**

218 In transgene assays, boundary elements block regulatory interactions when interposed been
219 enhancers (or silencers) and reporter genes (Chetverina *et al.*, 2014; Chetverina *et al.*, 2017;
220 Kellum and Schedl, 1992). To determine whether this is also true in their endogenous context,
221 we compared the expression in syncytial blastoderm embryos of the two genes that flank *nhomie*
222 at the *eve* locus, *eIF3j* and *CG12134*. As the *nhomie* deletion eliminates *homie*'s pairing partner
223 and disrupts the *eve* TAD, we also examined the expression of *eve* and of the gene just beyond
224 the *homie* boundary, *TER94*, which has strong maternal expression through stage 11 (Fig.
225 Supplemental 3B, WT). Consistent with the seemingly normal MicroC profile on the *homie* side
226 of the *eve* TAD, we did not detect evidence of *eve*-like *TER94* expression (Figs. 4 and 5). Thus,
227 the formation and functioning of the TM TAD does not appear to be impacted by the loss of
228 *nhomie* and the fact that left end of the *eve* TAD is no longer properly anchored.

229 In the case of the gene closest to the *nhomie* deletion, *CG12134*, we were unable to
230 consistently detect transcription driven by the *eve* enhancers in either *nhomie forward* or *λ DNA*
231 embryos. In some *λ DNA* embryos, there were hints of stripes at the blastoderm stage (see Fig.
232 Supplemental 2); however, these "stripes" were not observed in most embryos. Since *CG12134*
233 (which forms the TL4 sub-TAD in wild type) is closest to the *eve* enhancers and interacts most
234 strongly, it is possible that the promoter is not compatible with the *eve* enhancers. A different
235 result was obtained for *eIF3j* in *λ DNA* embryos. As shown in the HCR-FISH experiment in Fig.
236 4 and quantitated in Fig. 5, we observed a series of *eIF3j* stripes over a dark background in pre-
237 cellular blastoderm embryos. As this background hybridization is evident in earlier stages, much
238 of it is likely to be of maternal origin. In contrast to the *λ DNA* replacement, these stripes are not
239 visible in the *nhomie forward* (control) replacement (Figs 4 and 5). While it is possible to detect
240 all seven stripes in *λ DNA* blastoderm stage embryos, their levels of expression are not equal.
241 The highest levels correspond to *eve* stripes 1, 2, 3 and 7, while *eve* stripes 4, 5 and 6 are
242 expressed at much lower levels. Since the stripe enhancers for 1, 2, 3 and 7 are located between
243 the *eve* promoter and *nhomie*, they are closer to the *eIF3j* promoter than the enhancers for stripes
244 4, 5 and 6, which are located downstream of the *eve* transcription unit. In addition to possible
245 effects of distance, the subdomain linking the *eve* PRE and *homie* to the promoter is still
246 observed in the *λ DNA* replacement, and this could partially sequester the enhancers located
247 downstream of the *eve* promoter.
248 We also used digoxigenin *in situ* hybridization to analyze *eIF3j* expression. With this
249 procedure we were able to detect a very low level of *eve*-activated *eIF3j* stripe expression in WT
250 and *nhomie forward* embryos at stage 5 and stages 7-8 (Fig. Supplemental 3). In stage 5
251 embryos when *eve* expression is driven by specific stripe enhancers, *eIF3j* expression appears to
252 be similar in all seven stripes (Fig. Supplemental 3). In contrast, as was observed in the HCR-

253 FISH experiments (Fig. 4), there is a clear bias for enhancers located upstream of *eve* in the *λ*
254 *DNA* replacement at this point in development. In stage 7-8 embryos, the seven-stripe enhancer
255 drives *eve* expression. It is located close to *nhomie* and, not surprisingly, high levels of *eIF3j*
256 expression are observed in all seven stripes in the *λ DNA* replacement (Fig. Supplemental 3). At
257 later embryonic stages, *eve* expression is driven by tissue-specific neurogenic, mesodermal, and
258 anal plate enhancers. However, *eIF3j* is expressed at high levels in a complex pattern in older
259 embryos, and we were unable to unambiguously detect expression driven by the *eve* enhancers
260 over this background mRNA. This is also not surprising, given that all of the enhancers for these
261 aspects of *eve* expression are located downstream of the *eve* promoter, like the enhancers driving
262 stage 5 stripes 4, 5, and 6.

263 While the *nhomie* deletion did not have any obvious impact on the level or pattern of *eve*
264 expression in blastoderm stage embryos (see Fig. 4), it seemed possible that *eve* activity was not
265 entirely normal. To test this possibility, we mated males homozygous for either *λ DNA* or
266 *nhomie forward* to females heterozygous for a chromosomal deficiency that includes the *eve*
267 gene. We then quantitated the number of missing denticle bands in embryonic cuticle preps. As
268 shown in Fig. 5, the frequency of larvae with "severe" defects (2 or more missing ventral
269 denticle bands) in *nhomie forward* is similar to that in a WT *yw* control. In contrast, in the *λ*
270 *DNA* replacement, the frequency of larval cuticles with 2 or more missing denticle bands is
271 increased nearly two-fold. Taken together, the increase in severity of the cuticle defects is
272 significant at the $P > 0.01$ level (one-tailed t-test). The A6 denticle belt is missing most
273 frequently followed by A2, A4, and then A8. These even-numbered denticle bands are those that
274 are lost in *eve* deficiency mutants (from which the name *even skipped* comes), suggesting that
275 *eve* stripe expression at blastoderm stages is compromised in the embryos that produce these
276 defective cuticles.

277 ***The eve TAD is converted from a stem-loop to a circle-loop by inverting nhomie***

278 The orientation of boundary:boundary pairing interactions determines the topology of
279 each chromatin loop (Bing *et al.*, 2023; Fujioka *et al.*, 2016). Since *nhomie* and *homie* pair with
280 each other head-to-tail, the endogenous *eve* TAD is a stem-loop. This orientation dependence
281 means that one can convert the *eve* TAD from a stem-loop to a circle-loop by inverting the
282 *nhomie* boundary. If our expectations are correct, the MicroC contact pattern will also be
283 transformed from a volcano triangle with a plume to one in which sequences in the *eve* TAD is
284 surrounded by a cloud of crosslinked sequences from both neighboring TADs (TL and TM), like
285 that observed in the *Abd-B* region of BX-C.

286 We tested this prediction by inserting the *nhomie* boundary in the reverse orientation
287 (*nhomie reverse*). Fig. 6A shows that the *eve* TAD is reconstituted by *nhomie reverse* (compare
288 with Fig. 3). The sub-TAD evident in the *nhomie forward* replacement linking *nhomie* to the *eve*
289 promoter is also re-established (blue arrow). In addition, consistent with our expectation, the
290 plume topping the *eve* TAD is gone and is replaced by a much more sparsely populated LDC
291 domain (purple double arrow and above). The more prominent LDC TAD-TAD interactions (the
292 clouds) are between sequences in the *eve* TAD and the neighboring TADs. On the right, *eve*
293 forms an LDC interaction domain with TM (ev-TM). On the left, *eve* interacts strongly with
294 sequences in TL4, and progressively less strongly with sequences in the sub-TADs TL3, TL2,
295 and then TL1. In addition to restoring the *eve* TAD, the TL TAD is also re-established,
296 indicating that the *nhomie* boundary is important in defining both endpoints of the TL TAD. On
297 the other hand. with the exception of the *CG12133* sub-TAD, *nhomie* does not play a role in
298 generating the three other sub-TADs in the TL TAD. The other interesting feature is a 45° band
299 of interaction (to the left and below the purple double-arrow) between sequences in TL4 and
300 sequences in *eve* that appear to be located near the left edge of *homie*, and likely correspond to

301 the distal *eve* PRE (Fujioka *et al.*, 2008). A similar though weaker 45º band is also seen in
302 *nhomie forward* (Fig. 3).

303 ***Insulation is reduced in nhomie reverse***

304 Consistent with the models for stem-loops and circle-loops in Fig. 1, the neighborly
305 interactions evident in the MicroC contact patterns for *nhomie forward* and *nhomie reverse* are
306 quite distinct. The *nhomie forward* TAD is isolated from its neighbors, and crosslinking between
307 *eve* and the neighboring TADs is suppressed (Fig. 1B and 2A). This is not true for the circle-
308 loop TAD generated by *nhomie reverse*: in this configuration, the *eve* TAD is not sequestered
309 from neighboring TADs, but instead interacts much more frequently with sequences in next-door
310 TADs than in the stem-loop configuration. Since the *eve* TAD is no longer isolated from its
311 neighbors, this could increase the frequency of "productive" interactions between *eve* regulatory
312 elements and genes in nearby TADs, and vice versa.

313 To test whether the circle-loop topology has an impact on the regulatory landscape, we
314 hybridized *nhomie reverse* embryos with HCR-FISH probes for *eIF3j*, *TER94* and *eve*. In early
315 blastoderm stage *nhomie forward* embryos, there is little evidence of *eIF3j* or *TER94* expression
316 driven by *eve* stripe enhancers, and the HCR-FISH hybridization pattern is uniform (see Fig. 4).
317 In contrast, it is possible to discern individual stripes of both *eiF3j* and *TER94* mRNA over the
318 background signal in a subset of *nhomie reverse* blastoderm stage embryos in HCR-FISH (Fig.
319 7). Since these genes are assembled into their own topologically independent looped domains
320 rather than being in the same domain as *eve*, the level of *eiF3j* and also *TER94* stripe expression
321 is lower than that observed in the *nhomie* deletion (*λ DNA*). The *nhomie reverse* circle-loop also
322 differs from the *nhomie* deletion (*λ DNA*) in that there is not such an obvious preference for
323 which *eve* enhancers activate expression. In addition, *eve*-dependent *eiF3J* and *TER94* stripes are
324 detected in only about half of the blastoderm stage embryos (Fig. 5A). It is possible that the

325 frequency of productive inter-TAD contacts differs from one embryo to the next; however, a
326 more likely reason is that the high background of *eIF3j* and *TER94* transcripts obscures the low
327 level of *eve* enhancer-driven expression at this stage. Once the seven-stripe enhancer is
328 activated, *eve*-dependent *TER94* expression in *nhomie reverse* is elevated, and all seven stripes
329 are observed (Fig. Supplemental 3B). This fits with the MicroC contact profile. As shown in
330 Fig. 6, the *TER94* gene is preferentially crosslinked to *eve* sequences located between *nhomie*
331 *reverse* and the *eve* promoter as compared to sequences spanning the *eve* gene and the
332 downstream enhancers. By contrast, there is much less seven-stripe enhancer-driven expression
333 of *eIF3j* (Fig. Supplemental 3A) than *TER94*. Consistent with this observation, crosslinking
334 between *eIF3j* and sequences in *eve* close to *nhomie reverse* and the seven-stripe enhancer
335 appear to occur less frequently than crosslinking to sequences on the other side of the *eve* TAD
336 (though this crosslinking bias is not as pronounced as that observed between *TER94* and the *eve*
337 sequences near the seven-stripe enhancer relative to downstream *eve* sequences.)

338 While *eve* stripe expression is not discernably different from wild type, the circle-loop
339 topology still impacts *eve* function. As shown in Fig. 5B, the fraction of *nhomie reverse*
340 embryos with 2 or more missing denticle bands is nearly twice that in *yw* or the *nhomie forward*
341 replacement. Taken together, the increase in severity of the cuticle defects is significant at the P
342 > 0.01 level (one-tailed t-test). As was observed for the *λ DNA* replacement, the A6 denticle
343 band is missing most frequently, followed by A2, A4 and then A8.

344 ***homie forward converts the eve stem-loop to a circle-loop***

345 While the findings in the previous section show that loop topology impacts how
346 sequences in TADs interact with each other and with their neighbors, one might argue that the
347 effects we observed are a reflection of some novel properties of the *nhomie* boundary when it is
348 inverted. To test this possibility, we took advantage of the fact that in addition to pairing with

349 *nhomie*, the *homie* boundary pairs with itself (Fujioka *et al.*, 2016). However, unlike
350 *nhomie:homie* pairing which is head-to-tail, *homie:homie* pairing is head-to-head. This means
351 that it is possible to convert the *eve* TAD into a circle-loop by inserting *homie* into the *nhomie*
352 deletion in the forward orientation.

353 As shown in Fig. 6C, the MicroC contact profile of *homie forward* is similar to that
354 observed for *nhomie reverse*. The plume toping the *eve* TAD in wild type (Fig. 2) or in *nhomie*
355 *forward* (Fig. 4) is absent. Likewise, instead of being isolated from its neighbors, the *eve* TAD
356 contacts TL and TM. Also like *nhomie reverse*, *homie forward* forms a subdomain within the
357 *eve* TAD linking it to sequences in the *eve* promoter. There is also a 45° band of crosslinking
358 between sequences in TL4 and sequences on the distal side of *eve* that appears to correspond to
359 the *eve* 3' PRE.

360 The MicroC pattern is not the only similarity between *homie forward* and *nhomie*
361 *reverse*. The functional properties of the *homie forward eve* TAD are also similar. Fig. 7 shows
362 that the *eve* enhancers weakly activate both *eIF3j* and *TER94*. As was the case for *nhomie*
363 *reverse*, expression levels at the blastoderm stage are low and are observed in only about half of
364 the embryos (Fig. 5A). After the blastoderm stage, when the seven-stripe enhancer drives *eve*
365 expression, an even higher level of *TER94* expression is observed (Fig. Supplemental 3B). In
366 addition, the functioning of the *eve* gene when it is in the circle-loop configuration is not as
367 efficient, and the frequency of *homie forward* embryos with 2 or more missing denticle bands is
368 twice that of *nhomie forward* (Fig. 5B). Taken together, the increase in severity of the cuticle
369 defects is significant at the $P > 0.01$ level (one-tailed t-test).
370

371 **Discussion**

372 Two different though overlapping classes of chromosomal architectural elements have
373 been identified in flies. One class is the PREs found in many developmental loci. PREs were
374 first discovered because they induce pairing sensitive silencing of reporter genes (Americo et al.,
375 2002; Kassis et al., 1991). More recent studies have shown that the ability of these elements to
376 physically pair with each other may be their most important function (Batut *et al.*, 2022; Levo *et*
377 *al.*, 2022). The other class of architectural elements are chromatin boundaries (also called
378 insulators). PRE pairing in *cis* typically takes place within the context of a larger chromosomal
379 domain, or TAD. In contrast, boundary elements are responsible for defining the endpoints of
380 these looped domains (Arzate-Mejía et al., 2020; Batut *et al.*, 2022; Bing *et al.*, 2023; Chetverina
381 *et al.*, 2017; Ibragimov et al., 2023; Stadler et al., 2017). While not much is known about the
382 parameters governing PRE pairing, the pairing interactions of fly boundaries have been studied
383 in some detail. The key features include an ability to engage in promiscuous pairing interactions,
384 distinct partner preferences, and orientation dependence. Of the endogenous (non-*gypsy*)
385 boundaries whose functional properties have been studied in detail, only one, *Fab-7*, appears to
386 be able to pair in both orientations. However, *Fab-7* may be unusual in that its boundary activity
387 depends upon factors that have been implicated in the functioning of PREs (Kyrchanova et al.,
388 2018). For all of the other boundaries studied so far, pairing interactions are orientation
389 dependent. When fly boundaries pair with themselves, the interactions are head-to-head
390 (Kyrchanova *et al.*, 2008a). This make sense, as the available evidence suggests that self-pairing
391 interactions in *trans* may be largely responsible for the pairing of homologs in precise register
392 (Erokhin et al., 2021; Fujioka *et al.*, 2016). In this case, head-to-tail self-pairing would
393 uncoupled the loops on the two homologs.

394 Unlike self-pairing in *trans*, pairing interactions between heterologous boundaries in *cis*
395 can be head-to-head or head-to-tail. The topological consequences are quite distinct. The former
396 generates a circle-loop, while the later forms a stem-loop (Chetverina *et al.*, 2017). In the
397 studies reported here, we have investigated how these two different topologies impact the local
398 chromatin organization. We have also determined whether circle-loops and stem-loops alter the
399 ability of boundary elements to define units of independent gene activity and insulate against
400 regulatory interactions between neighboring TADs.

401 *nhomie deletion disrupts the eve TAD*

402 As would be predicted from many different studies (c.f., (Cavalheiro *et al.*, 2021;
403 Chetverina *et al.*, 2017), deletion of the *nhomie* boundary and replacement with a control *λ DNA*
404 disrupts the *eve* TAD and alters the regulatory landscape. The MicroC profile shows that
405 disruption of the *eve* TAD and the neighboring TADs is one sided. Within the *eve* TAD, the
406 subdomain linking *homie* and the nearby PRE to the *eve* promoter is unaffected. Likewise the
407 large TAD, TM, which encompassess both *TER94* and *pka-R2*, and is defined at one end by
408 *homie* and at the other by an uncharacterized boundary element upstream of the *pka-R2*
409 promoter, is intact (Fig. Supplemental 1B). In contrast, on the *nhomie* side of the *eve* TAD, the
410 sub-TAD linking *nhomie* to the *eve* promoter is absent, and is replaced by a less well-defined
411 sub-TAD linking the *eve* promoter to an element near the *CG12134* promoter. However, the
412 end-point of the *eve* TAD is no longer distinct, and *eve* sequences are now crosslinked to the
413 *eIF3j* sub-TAD and to sequences in the more distant TL sub-TADs, TL3, TL2 and TL1.
414 Consistent with the alterations in the physical organization of the *eve* and neighboring TADs, the
415 *TER94* gene is still insulated from the *eve* enhancers. While sequences in the *eve* TAD
416 physically interact with the gene closest to *nhomie*, *CG12134*, only the next gene over, *eIF3j*, is
417 clearly activated by the *eve* enhancers. Since crosslinking between sequences in the *CG12134*

418 and the *eve* TAD is more frequent than crosslinking between the *eIF3j* sub-TAD TL3 and the *eve*
419 TAD, it seems likely that *CG12134* is refractory to activation by the *eve* enhancers. This could
420 be due to an incompatiblity between the *CG12134* promoter and the *eve* enhancers.
421 Alternatively, the promoter may not be active at this stage. While *eIF3j* is activated by the *eve*
422 enhancers in stage 5 embryos in the *nhomie* deletion, the stripe enhancers located upstream of the
423 *eve* gene drive a higher level of expression than those located downstream. Two factors in
424 addition to the effects of distance could potentially account for this finding. Since the *eve*
425 promoter is located between the downstream enhancers and the *eIF3j* gene, activation of *eIF3j*
426 by the downstream enhancers could be suppressed by promoter competition. Alternatively, or in
427 addition, the sub-TAD formed between the 3' PRE/*homie* and the *eve* promoter/proximal PRE
428 (Fujioka *et al.*, 2008) could tend to sequester the downstream *eve* stripe enhancers away from
429 interactions with *eIF3j*.
430 *Topology impacts local 3D genome organization and the potential for regulatory interactions*
431 In boundary bypass experiments using endogenous fly boundaries, the ability of the
432 upstream enhancers to activate the downstream reporter depended on the topology of the loop
433 generated by the paired boundaries (Kyrchanova *et al.*, 2008a). Activation is observed for stem-
434 loops, as this configuration brings the upstream enhancers into close proximity with the
435 downstream reporter. In contrast, the enhancers and downstream reporter are not brought into
436 contact when the topology is a circle-loop. As would be predicted from these bypass
437 experiments, the stem-loop formed by the head-to-tail pairing of *nhomie* and *homie* physically
438 isolates the *eve* TAD from its neighbors, and this is reflected in the low density of contacts
439 between sequences in *eve* and the neighboring TADs (Fig. 2A). Conversely, the TADs that flank
440 *eve* are brought together and contacts between them generate the plume that is observed above
441 the *eve* volcano triangle.

442 The physical isolation afforded by the stem-loop topology is lost when the *eve* TAD is
443 converted to a circle-loop, either by inverting the *nhomie* boundary or by replacing *nhomie* with
444 the *homie* boundary inserted in the forward direction (Fig. 6). In the former case, head-to-tail
445 *nhomie*:*homie* pairing generates a circle-loop. In the later case, head-to-head pairing of *homie*
446 (inserted in the forward orientation) with endogenous *homie* generates a circle-loop. The
447 alteration in the local 3D organization induced by the conversion of *eve* to a circle-loop is
448 evident from the changes in the MicroC contact pattern. Instead of being isolated from
449 neighboring TADs, the *eve* TAD interacts not only with its immediate neighbors, but also with
450 more distant TADs. As a result, the plume of enhanced contacts linking TM to TL, TK, and TJ
451 is absent and is replaced by contacts between these TADs and the *eve* TAD.
452 As might be expected from the MicroC contact patterns, the conversion to a circle-loop
453 topology is accompanyied by alterations in regulatory interactions between *eve* and the genes in
454 the neighboring TADs (Fig. 7 and Fig. Supplemental 3). Unlike the *nhomie forward*
455 replacement, the *eve* stripe enhancers in both of the circle-loop replacements are able to weakly
456 activate expression of two neighboring genes, *eIF3j* and *TER94*. This pattern of activation
457 mirrors the enhancement in contacts between the *eve* TAD and the neighboring TL and TM
458 TADs evident in MicroC experiments. Thus, though *eIF3j* and *TER94* are clearly shielded from
459 the *eve* enhancers when the *eve* TAD is a circle-loop, a greater degree of isolation from the
460 action of the *eve* enhancers is afforded when the *eve* TAD is a stem-loop.
461 In addition to reducing insulation from regulatory interactions with genes in neighboring
462 TADs, the circle-loop topology impacts the functioning of the *eve* gene (Fig. 5B). For both
463 *nhomie reverse* and *homie forward*, the frequency of multiple denticle band defects compared to
464 the *nhomie forward* control is enhanced in a sensitized genetic background. While we did not
465 detect any obvious reductions in the *eve* stripes in blastoderm stage embryos, the circle-loop

466 provides less insulation than the stem-loop, and it is possible that the neighboring promoters
467 suppress *eve* expression by competing for the *eve* enhancers. Another (non-mutually exclusive)
468 possibility comes from the studies of Yokoshi et al. (Yokoshi et al., 2020), who used live
469 imaging to examine the effects of flanking a reporter with the *nhomie* and *homie* boundaries. In
470 their experiments, reporter expression was enhanced over two-fold when the reporter was
471 flanked by *nhomie* and *homie*; however, the enhancement was greater when the paired
472 boundaries formed a stem-loop than when they formed a circle-loop.

473 *Stem-loops versus circle-loops*

474 The results we have reported here raise several questions. One of these is, what is the
475 relative frequency of stem-loops versus circle-loops in the fly genome? The MicroC contact
476 patterns for the stem-loop and circle-loop versions of the *eve* TAD are quite distinct. The former
477 is a volcano triangle with a plume while the latter is a volcano triangle flanked by clouds. A
478 survey of the MicroC contact patterns elsewhere in the non-repetitive regions of the fly genome
479 indicates that volcanoes with plumes are rare (~30). For example, there are two volcano triangles
480 with plumes in the *Antennapedia* complex and they encompass the *deformed* and *fushi-tarazu*
481 genes (Levo *et al.*, 2022). However, since most of the "euchromatic" regions of the fly genome
482 are assembled into TADs whose MicroC profiles resemble that observed for *eve* circle-loops and
483 the *Abd-B* region of BX-C, it possible that much of the fly genome is assembled into circle-
484 loops, not stem-loops.

485 While this suggestion is consistent with the available data, it is based on contact patterns
486 between neighboring TADs, and important caveats remain. For one, the contact patterns
487 between neighboring TADs can deviate in one way or another from that seen in the *Abd-B*
488 region. For example, there are TADs in which interactions with one set of neighbors appears to
489 be suppressed as expected for stem-loops, but the classic plume is absent, as interactions are not

490 suppressed with the other neighbors (c.f., Fig. Supplemental 4A). In other cases, there are a
491 series of complicated TAD-TAD interactions topped by a rectangular plume (Fig. Supplemental
492 4B: purple arrow). For this reason, it will not be possible to draw firm conclusions about the
493 frequency of stem-loops versus circle-loops genome-wide until the relative orientation of the
494 paired boundaries themselves can be determined directly. On the other hand, it is clear from our
495 studies that both classes of TADs must exist in flies. If, as seems likely, a significant fraction of
496 the TADs genome-wide are circle-loops, this would effectively exclude cohesin-based loop
497 extrusion as a general mechanism for TAD formation in flies. In addition, though stem-loops
498 could be generated by a cohesin-dependent mechanism, it is unlikely that this mechanism is
499 operational in flies, as we have shown here and in Bing et al. (Bing *et al.*, 2023) that stem-loops
500 in flies are formed by orientation-dependent boundary:boundary pairing.
501 Another important question is whether our findings have any relevance to the formation
502 and topology of TADs in mammals. In the most common version of the loop extrusion model,
503 the mammalian genome is assembled into an alternating pattern of stem-loops and unanchored
504 loops (c.f., (Davidson and Peters, 2021; Higashi and Uhlmann, 2022; Perea-Resa et al., 2021).
505 In this case, one might expect to observe volcano triangles topped by plumes alternating with
506 DNA segments that have a considerablly lower densisty of internal contacts. However, this
507 crosslinking pattern is not observed in published MicroC data sets (Hsieh et al., 2020;
508 Krietenstein et al., 2020). Instead of an alternating pattern of high-density TAD triangles
509 separated by regions of low density contacts, the TAD triangles are generally linked to both
510 neighbors, just as in flies. Moreover, also like in Drosophila, there are very few stem-loop
511 volcano TADs topped by plumes. Instead, the crosslinking pattern between neighboring TADs
512 appears similar to that observed for circle-loops in flies. Of course, one problem with these
513 MicroC studies is that the resolution may not be sufficient to detect volcanos with plumes or the

514 other features predicted by the loop extrusion model. However, there are no obvious volcanoes
515 with plumes in the much higher resolution RCMC studies of Goel et al. (Goel et al., 2023).
516 Instead the MicroC profiles most closely resemble those seen in the *Abd-B* region of BX-C (c.f.
517 the *Ppm1g* locus in Fig. 4 of Goel et al., (Goel *et al.*, 2023)). Moreover, compromising cohesin
518 activity has minimal impact on the TADs in this region of the mouse genome, as evidenced from
519 the MicroC pattern before and after knockdown. Based on these observations, one can
520 reasonably question whether cohesin-mediated loop extrusion is deployed in mammals as the
521 mechanism for not only generating TADs but also determining TAD boundaries. Clearly
522 validation of the loop extrusion/CTCF road-block model as currently formulated will require a
523 direct demonstration that mammalian TADs are exclusively either stem-loops or unanchored
524 loops, and that the endpoints are always (or almost always) determined by CTCF roadblocks.
525

526 **Acknowledgements:** We would like to thank the Gordon Grey for running the fly food
527 facility at Princeton, members of the Lewis Sigler Genomics Core facility for their invaluable
528 assistance with DNA sequencing, and Qing Liu for excellent technical assistance. We would
529 also like to thank members of MOL431 for creative input. Special thanks to Olga Kyrchanova,
530 Daria Chetverina, Maksim Erokhin, Pavel Georigev, Tsutomu Aoki, Girish Deshpande, Airat
531 Ibragimov, Sergey Ryabichko, Yuri Pritykin, Alex Ostrin, Xinyang Bing, Xiao Li and Mike
532 Levine for stimulating discussions and sharing unpublished data.
533

534 # Materials and methods

535

536 **Key resources table**

REAGENT or RESOURCE	SOURCE	IDENTIFIER
Chemicals, peptides, and recombinant proteins		
n-Heptane	Fisher Chemical	O3008-4
Paraformaldehyde 20% solution, EM Grade	Electron Microscopy Sciences	15713-S
Formaldehyde, 16%, methanol free, Ultra Pure	Polysciences Inc	18814-10
PBS - Phosphate-Buffered Saline (10X) pH 7.4, RNase-free	Thermal Fisher	AM9624
Tween 20	Sigma	P1379
Triton X-100	Bio-Rad	161-0407
Tris base	Sigma	11814273001
Methanol	Fisher Chemical	203403
SSC, 20X	Thermal Fisher	15557044
Formamide	Thermal Fisher	17899
Dextran sulfate	Sigma	D8906
Salmon Sperm DNA	Thermal Fisher	AM9680
Ribonucleoside Vanadyl Complex	NEB	S1402S
Nuclease-free BSA	Sigma	126609
Triethylammonium Acetate	Sigma	625718
dGTP (100 MM)	VWR	76510-208
dTTP (100 MM)	VWR	76510-224
Lonza NuSieve 3:1 Agarose	Thermal Fisher	BMA50090
T4 DNA ligase	NEB	M0202L
Biotin-11-dCTP	Jen Bioscience	NU-809-BIOX

Biotin-14-dATP	Jen Bioscience	NU-835-BIO14
Qubit dsDNA HS Assay Kit	Life Technologies Corporation	Q32851
Atto 633 NHS ester	Sigma	01464
Phase Lock Gel™, QuantaBio - 2302830, Phase Lock Gel Heavy	VMR	10847-802
NEBNext Ultra II DNA Library Prep Kit for Illumina	NEB	E7645S
Ampure Xp 5ml Kit	Thermal Fisher	NC9959336
Hifi Hotstart Ready Mix	Thermal Fisher	501965217
Dynabeads MyOne Streptavidin C1	Life Technologies Corporation	65001
cOmplete™, EDTA-free Protease Inhibitor Cocktail	Sigma	11873580001
N,N-Dimethylformamide	Sigma	227056
Potassium acetate solution	Sigma	95843
DSG (disuccinimidyl glutarate)	Thermal Fisher	PI20593
T4 Polynucleotide Kinase - 500 units	NEB	M0201S
DNA Polymerase I, Large (Klenow) Fragment - 1000 units	NEB	M0210L
End-it DNA End Repair Kit	Thermal Fisher	NC0105678
Proteinase K recomb. 100 mg	Sigma	3115879001
Nuclease MicroCoccal (s7)	Thermal Fisher	NC9391488
EGS (ethylene glycol bis(succinimidyl succinate))	Thermal Fisher	PI21565
Atto 565 NHS ester	Sigma	72464
HCR™ RNA-FISH Custom Probe Set: eve	Molecular Instruments	
HCR™ RNA-FISH Custom Probe Set: ter94	Molecular Instruments	
HCR™ RNA-FISH Custom Probe Set: CG12134	Molecular Instruments	
HCR™ RNA-FISH Custom Probe Set: eIF3j	Molecular Instruments	

HCR™ Amplifier B1, 488	Molecular Instruments	
HCR™ Amplifier B2, 564	Molecular Instruments	
HCR™ Amplifier B3, 647	Molecular Instruments	
HCR™ Buffers	Molecular Instruments	
NEBNext Multiplex Oligos for Illumina	NEB	E7335S
Software and algorithms		
Fiji (ImageJ)	Schindelin et al., 2012	fiji.sc
NIS element	Nikon	microscope.healthcare.nikon.com/products/software/nis-elements
Graphpad Prism 8	GraphPad Software	graphpad.com
HiGlass	Kerpedjiev et al., 2018	higlass.io
bwa	Li H. and Durbin R., 2009	bio-bwa.sourceforge.net/
samtools	Github/open source	samtools.github.io
pairsamtools	Github/open source	github.com/mirnylab/pairsamtools
pairix	Github/open source	github.com/4dn-dcic/pairix
cooler	Abdennur, N., and Mirny, L., 2019	github.com/mirnylab/cooler
Miniconda	Anaconda	docs.conda.io/en/latest/miniconda.html
Snakemake	Github/open source	snakemake.github.io

537 **Creation of *nhomie* deletion flies**

538 To modify *nhomie* at the *eve* locus, we used recombinase-mediated cassette exchange
539 (Bateman et al., 2006). First, we inserted two nearby attP sites, using CRISPR. The donor
540 plasmid for this was constructed as follows. First, a mini-*white* (*mw*) gene with Glass binding
541 sites (Fujioka et al., 1999) was inserted into BlueScript. From the standard *mw* gene, the Wari
542 insulator (Chetverina et al., 2008) was deleted. Then, two 102bp attP sequences (Venken et al.,
543 2011) were inserted, one just 5' of the Glass binding sites and the other at the 3' end of the
544 modified *mw*, creating the plasmid P-attPx2-*mw*. 5' and 3' homologous arms were added to both
545 ends. Two gRNA sequences were cloned into plasmid pCFD4 ((Port et al., 2014), Addgene).
546 The donor and gRNA plasmids were injected into a Cas9 line (y[1] M{vas-Cas9.S}ZH-2A
547 w[1118]), Bloomington Drosophila Stock Center). This chromosomal modification resulted in
548 one attP site being inserted in the intron of *CG12134*, and the other being inserted between the
549 *eve* 7-stripe enhancer and the 3+7 stripe enhancer regions. This also deleted 2.2kb of
550 endogenous sequence, including *nhomie* and the *eve* 7-stripe enhancer.

551 After identifying a successful insertion (NattPmw), *mw* was replaced by each of the
552 following using RMCE: 1) the previously deleted 2.2kb, restoring *nhomie* and the *eve* 7-stripe
553 enhancer, to create "wild-type *nhomie*" (*nhomie forward*), 2) the same 2.2kb sequence, but with
554 600bp of phage λ DNA in place of 600bp *nhomie* (λ DNA), 3) the same 2.2kb sequence, but
555 with 600bp *nhomie* inverted (*nhomie reverse*), and 4) the same 2.2kb sequence, but with 600bp
556 *nhomie* replaced by a copy of ~600bp *homie* in its native orientation in the chromosome (*homie*
557 *forward*). Each of these changes was confirmed by sequencing of genomic DNA from the
558 transgenic fly lines.

559 **Analysis of embryonic cuticle patterns and *in situ* hybridization**

560 To identify defects in developing embryos, embryos were collected for 2.5 hr., and
561 allowed to develop for an additional 20-21 hr. at 25°C. Embryos were dechorionated and
562 mounted in a 1:1 mixture of Hoyer's medium and lactic acid. Mounted embryos were left at
563 room temperature until they cleared (12-14 days), and the patterns of ventral abdominal denticles
564 were examined and tallied as follows. Loss of at least one-fifth of a denticle band (in A1-A8)
565 was counted as "missing". Fused denticle bands, which rarely occurred, was also counted as a
566 "missing" band. Minor defects such as in individual denticle rows were not counted.

567 Digoxigenin (DIG) *in situ* hybridization was performed using DIG-labeled anti-sense
568 RNA against *CG12134*, *eIFj3*, and *TER94*. RNA expression was visualized using alkaline
569 phosphatase-conjugated anti-DIG antibody (Roche), using CBIP and NBT as substrates (Roche).
570 Each set of experiments was carried out in parallel to minimize experimental variation.
571 Representative expression patterns are shown in each figure.

572

573 **HCR-FISH**

574 The sequences of target genes were obtained from Flybase (flybase.org)(Gramates et al., 2022).
575 To design probes, the target gene sequences were submitted to the Molecular Instruments probe
576 design platform (www.molecularinstruments.com/hcr-rnafish) (Choi et al., 2016), with
577 parameters set to a 35 probe set size for *Drosophila melanogaster*. A similar method was
578 designed based on published smFISH methods (Little and Gregor, 2018; Trcek et al., 2017). 100-
579 200 flies were placed in a cage with an apple juice plate at the bottom of the cage. For early
580 stages, the embryos were collected for 7 hours, while for later-stage embryos, collection were
581 overnight. Embryos from each plate were washed into collection mesh and dechorionated in
582 bleach for 2min, then fixed in 5mL of 4% paraformaldehyde in 1X PBS and 5mL of heptane for

583 15min with horizontal shaking. The paraformaldehyde was then removed and replaced with
584 5mL methanol. The embryos were then devitellinized by vortexing for 30s, and washed in 1mL
585 of methanol twice. Methanol was then removed and replaced by PTw (1X PBS with 0.1%
586 Tween-20) through serial dilution as 7:3, 1:1, and 3:7 methanol:PTw. The embryos were washed
587 twice in 1mL of PTw and pre-hybridize in 200µL of probe hybridization buffer for 30 min at 37°
588 C. 0.4pmol of each probe sets were added to the embryos in the probe hybridization buffer and
589 the embryos were incubated at 37ºC for 12-14h. The embryos were then washed 3X with probe
590 wash buffer at 37°C for 30min and 2X with 5X SSCT(5X SSC+0.1% tween) at room
591 temperature for 5min. Then the embryos were pre-amplify with 300µL amplification buffer for
592 10 min at 25°C. Meanwhile, 6 pmol of hairpin h1 and h2 were snap cooled separately (95ºC for
593 1:30, cool to RT with 0.1ºC drop per second), and then mixed in 100µL of amplification buffer
594 at room temperature. After that, the pre-amplification solution was removed from the embryos,
595 and 100µL of hairpin h1/h2 mix were added to the embryos. Next, the embryos were incubated
596 for 12-14h at room temperature in dark. To remove the excess hairpins, the embryos were then
597 washed in SSCT as follows: 2X for 5min, 2X for 30min and 5X for 5min. Then, the embryos
598 were washed with 1mL PTw for 2min and stained with DAPI/Hoechst at 1µg/mL for 15min at
599 room temperature in the dark. The embryos were then washed with PTw 3X for 5min. Finally,
600 the embryos were mounted on microscope slides with Vectashield and a #1.5 coverslip for
601 imaging.
602
603 **Imaging, image analysis and statistics**
604 Embryos from hcrFISH were imaged by using a Nikon A1 confocal microscope system,
605 Plan Apo 20X/0.75 DIC objective. Z-stack images were taken at interval of 2µm, 4X average,
606 1024X1024 resolution, and the appropriate laser power and gain were set for 405, 488, 561, and

607 640 channels to avoid overexposure. Images were processed by ImageJ and the maximum
608 projection was applied to each of the stack images. To determine the presence of stripes of early
609 embryos, multi-channel images were first split into single channels and the stripe signal was
610 highlighted and detected by the MaxEntropy thresholding method. GraphPad Prism was used for
611 data visualization and statistical analysis. Two-way ANOVA with Tukey's multiple
612 comparisons test for each pair of groups was used to determine the statistical significance for the
613 percentage of embryos carrying stripes in *eIF3j* and *TER94* channels in each group.

614 **MicroC library construction for the *nhomie* replacements**

615 Embryos were collected on yeasted apple juice plates in population cages for 4 hours,
616 incubated for 12 hours at 25°C, then subjected to fixation as follows. Embryos were
617 dechorionated for 2min in 3% sodium hypochlorite, rinsed with deionized water, and transferred
618 to glass vials containing 5mL PBST (0.1% Triton-X100 in PBS), 7.5mL n-heptane, and 1.5mL
619 fresh 16% formaldehyde. Crosslinking was carried out at room temperature for exactly 15min
620 on an orbital shaker at 250rpm, followed by addition of 3.7 mL 2M Tris-HCl pH7.5 and shaking
621 for 5min to quench the reaction. Embryos were washed twice with 15mL PBST and subjected to
622 secondary crosslinking. Secondary crosslinking was done in 10mL of freshly prepared 3mM
623 final DSG and ESG in PBST for 45min at room temperature with passive mixing. The reaction
624 was quenched by addition of 3.7mL of 2M Tris-HCl pH7.5 for 5min, washed twice with PBST,
625 snap-frozen, and stored at -80°C until library construction.
626 Micro-C libraries were prepared as previously described (Batut *et al.*, 2022) with the following
627 modifications: 50µL of 12-16h embryos were used for each biological replicate. 60U of MNase
628 was used for each reaction to digest chromatin to a mononucleosome:dinucleosome ratio of 4.
629 Libraries were barcoded, pooled and subjected to paired-end sequencing on an Illumina Novaseq
630 S1 100nt Flowcell (read length 50 bases per mate, 6-base index read).

631 **Micro-C data processing**

632 MicroC data for *D. melanogaster* were aligned to custom genomes edited from the
633 Berkeley Drosophila Genome Project (BDGP) Release 6 reference assembly (dos Santos et al.,
634 2015) with BWA-MEM (Li and Durbin, 2009) using parameters **-S -P -5 -M**. The resultant
635 BAM files were parsed, sorted, de-duplicated, filtered, and split with Pairtools
636 (https://github.com/mirnylab/pairtools). We removed pairs where only half of the pair could be
637 mapped, or where the MAPQ score was less than three. The resultant files were indexed with
638 Pairix (https://github.com/4dn-dcic/pairix). The files from replicates were merged with Pairtools
639 before generating 100bp contact matrices using Cooler (Abdennur and Mirny, 2020). Finally,
640 balancing and Mcool file generation was performed with Cooler's Zoomify tool.

641 Virtual 4C profiles were extracted from individual replicates using FAN-C (Kruse et al.,
642 2020) at 400bp resolution. The values were summed across replicates and smoothed across three
643 bins (1.2kb). The *homie* Viewpoint was set to the 549nt *homie* sequence that was defined in
644 previous studies.

645

646 **Figure Legends**

647 **Figure 1. Diagram of the possible loop topologies generated by head-to-head and head-to-**
648 **tail pairing.** A) Head-to-tail boundary (arrows) pairing generates a series of stem-loops linked
649 together by unanchored loop. In this case, the main axis of the chromosome would correspond to
650 the unanchored loops connecting different stem-loops. B) If boundaries pair with both neighbors
651 (head-to-tail) the stem-loops would be linked to each other by the paired boundaries. In this case
652 the main axis of the chromosome will correspond to the paired boundaries. C) Head-to-head
653 boundary pairing generates a series of circle-loops linked together by an unanchored loop. The
654 unanchored loop will be the main axis of the chromosome. D) If boundaries pair with both
655 neighbors (head-to-head), the chromatin fiber will be organized into a series of circle-loops
656 connected to each other at their base and these paired boundaries will define the chromosomal
657 axis. In both B) and D), the pairing interactions between the blue and red boundaries need not be
658 in register with the pairing of the red boundary to the next-door green boundary. In this case, the
659 main axis of the chromosome may bend and twist, and this could impact the relative orientation
660 of the stem-loops/circle-loops. More complex structures would be generated by mixtures of
661 stem-loops and circle-loops.
662
663 **Figure 2. Stem-loops and circle-loops.** "*Once in a while you get shown the light in the*
664 *strangest of places if you look at it right*." * MicroC contact profile for *Drosophila* wild-type
665 (*yw*) stage 14 embryos. A) *eve* and neighboring TADs (TI, TJ, TK TL, TM and TN). The *eve*
666 TAD is a volcano with a plume that is anchored by *nhomie* (*nh*) and *homie* (*h*). The plume is
667 generated by crosslinking of sequences in neighboring TADs. At the bottom of the plume, TL
668 sequences are linked to sequences in TM close to *eve* including *ter94*. At the next level,
669 sequences in TK are linked to TM. In addition, sequences in LM are linked to sequences in TM
670 located beyond the *TER94* gene. At the next level, sequences in TJ are linked to sequences in
671 TM. Note that interactions between sequences in TL and TJ and sequences in TM close to the
672 *eve* TAD are somewhat less frequent than those farther away from the *eve* TAD. Sequences in
673 the neighboring TAD also interact with each other as indicated. For example, sequences in TK
674 and TJ interact with each other (J-K) and also with interact with sequences in TI (I-K and I-J).
675 B) The Bithorax *Abd-B* gene and the parasegment (PS) specific regulatory domains, *iab-3, iab-4,*
676 *iab-5*, *iab-6*, *iab-7*, *iab-8*. *iab-4* regulates the *abd-A* gene in PS9. *iab-5* regulates *Abd-B* in
677 PS10, *iab-6* regulates *Abd-B* in PS11, *iab-7* regulates *Abd-B* in PS12 and *iab-8* regulates *Abd-B*
678 in PS13. The domains are separated from each other by the boundary elements *Fab-4*, *Mcp*,
679 *Fab-6*, *Fab-7*, and *Fab-8* as indicated. The *AB-I* boundary is located upstream of the *Abd-B*
680 promoter. Each regulatory domain corresponds to a TAD. Though insulated from each other,
681 each TAD interacts with its immediate neighbor. For example, *iab-5* interacts with its immediate
682 neighbor *iab-4* and *iab-6* to give *4-5* and *5-6* respectively. It also interacts with the next-next
683 door neighbor *iab-7* (*5-7*) and even its next-next-next door neighbor *iab-8* (*5-8*). (x: Scarlet
684 Begonias GD: 1974).
685
686 **Figure 3. TAD organization of the *nhomie forward* and *λDNA* replacements.** A) MicroC
687 contact profile of stage 14 *nhomie forward* embryos. In this replacement *nhomie* is inserted in
688 the same orientation as the endogenous *nhomie*. N(replicates)=2. Resolution = 200bp. *L-M*:
689 Interactions between TADs TL and TM flanking the *eve* locus. Asterisk: sub-TAD linking the
690 *eve* promoter to the *eve* PRE and *homie*. Dark blue arrow: sub-TAD linking the *eve* promoter to
691 *nhomie*. Light blue arrowhead: *nhomie*. Red arrowhead: *homie*. Green arrowhead: sub-TAD
692 boundary formed by the *CG12134* promoter region. Dark blue arrowhead: sub-TAD boundary

693 formed by *eIF3j* promoter region. Diagram: Map of *eve* locus and surrounding genes. B)
694 Virtual 4C with viewpoint from *homie* (black arrow) towards *nhomie forward*. C) Diagram of
695 the *eve* stem-loop TAD. D) MicroC contact profile of stage 14 *λ DNA* embryos. In this
696 replacement, λ DNA is inserted in place *nhomie*. N(replicates)=2. Resolution = 200bp. Asterisks:
697 sub-TAD linking the *eve* promoter to the *eve* PRE and *homie*. Purple arrowhead: sub-TAD
698 linking *CG12134* promoter region to *eve* promoter. The *eIF3j* sub-TAD (demarked by the blue
699 and green arrowheads) is still present. E) Virtual 4C with viewpoint from *homie* reading toward
700 *eIF3j*. F) Diagram of the "unanchored" *eve* TAD. Arrows show novel interactions.
701
702 **Figure 4. *nhomie* deletion (*lambda DNA* replacement) exposes *eIF3j* to the *eve* enhancers.**
703 *nh forward*: *nhomie* replacement with *nhomie* in the forward (WT) orientation. *λ DNA: nhomie*
704 replacement with λ DNA. At the syncytial blastoderm stage, a series of stripe-specific enhancers
705 upstream (stripes 1, 2, 3, 7) and downstream (stripes 1, 4, 5, 6) of the *eve* gene drive *eve*
706 expression. During cellularization of the blastoderm and gastrulation, a single enhancer located
707 upstream of *eve* drives expression of all seven stripes. DAPI: DNA stained with DAPI (blue).
708 *eIF3j*: Embryo hybridized with probe complementary to *eIF3j* mRNA. *eve*: Embryo hybridized
709 with probe complementary to *eve* mRNA. *TER94*: Embryo hybridized with probe
710 complementary to *TER94*. Yellow carets: *eve*-enhancer-driven *eIF3j* stripes. Control non-
711 specific probes for each channel indicates autofluorescence background for each channel in the
712 top panel.
713
714 **Figure 5. Manipulating the *nhomie* boundary impacts the regulatory landscape.** N=# of
715 independent replicate, n= # of embryos. Two-way ANOVA with Tukey's multiple comparisons
716 test for each pair of groups was used to determine the statistical significance. *p≤ 0.05,
717 **p≤0.01, ***p≤0.001 and ****p≤0.0001. A) Quantitation of numbers of embryos showing
718 stripe patterns in HCR-FISH for *eIF3j* and *TER94,* as shown in Fig. 4 and Fig 7. N=3. n=45 for
719 each group. B) Quantitation of the number of missing ventral denticle bands in larvae from a
720 cross of *BSC/CyO,hb-lacZ* deficiency females to males of the indicated genotypes (N=6): wild-
721 type control (*yw*) n = 767. The *nhomie forward* replacement n = 1099. The *λDNA* replacement n
722 = 1175. The *nhomie reverse* replacement: n = 1083. The *homie forward* replacement: n =
723 1137.
724
725
726 **Figure 6. TAD organization of the *nhomie reverse* and *homie forward* replacements.** A)
727 MicroC contact profile of stage 14 *nhomie reverse* embryos. In this replacement *nhomie* is
728 inserted in the reverse orientation compared to WT *nhomie*. N(replicates)=2. Resolution =
729 200bp. B) Virtual 4C with viewpoint from *homie* (black arrow) towards *nhomie reverse*. C)
730 MicroC contact profile of stage 14 *homie forward* embryos. In this replacement *homie* is
731 inserted in the forward orientation (the same as the endogenous *homie*). N(replicates)=2.
732 Resolution = 200bp. D) Virtual 4C with viewpoint from *homie* (black arrow) towards *homie*
733 *forward*. A) and C) Note that interactions between the TADs flanking the *eve* locus (purple
734 double arrow) are suppressed compared to *nhomie forward* (see Fig. 3), while interactions
735 between *eve* and TL, TM are enhanced (L-ev and ev-M). Asterisks: sub-TAD linking the *eve*
736 promoter to the *eve* PRE and *homie*. Dark blue arrow: sub-TAD linking the *eve* promoter to
737 *nhomie reverse*. Light blue bar: *nhomie reverse*. Red bar: *homie*. Green arrowhead: sub-TAD
738 boundary formed by the *CG12134* promoter region. Dark blue arrowhead: sub-TAD boundary
739 formed by the *eIF3j* promoter region. Diagram: Map of *eve* locus and surrounding genes.
740

741
742 **Figure 7. *eve* enhancers activate neighboring genes when the *eve* TAD is a circle-loop.**
743 hcrFISH hybridization to mRNA expressed by *eIF3j*, *eve* and *TER94* at the blastoderm stage
744 (embryonic stage 5). *nh forward*: *nhomie* replacement with *nhomie* in forward (normal)
745 orientation (same as in Fig. 3). *nh reverse: nhomie* replacement with *nhomie* in reverse
746 orientation. *h forward: nhomie* replacement with *homie* in forward orientation. Yellow
747 arrowhead: position of stripes. DAPI (blue): DNA stained with DAPI. *eIF3j* (green): Embryo
748 hybridized with probe complementary to *eIF3j* mRNA. *eve* (orange): Embryo hybridized with
749 probe complementary to *eve* mRNA. *TER94* (red): Embryo hybridized with probe
750 complementary to *TER94*. Control non-specific probes for each channel indicates
751 autofluorescence background for each channel in the top panel.
752
753
754
755
756
757
758 **Figures Supplemental**
759
760 **Fig. Supplemental 1. MicroC contact profiles for *nhomie forward*, *λDNA*, *nhomie reverse*,**
761 **and *homie forward* in larger scale.** N(replicates)=2. Resolution=200. A) MicroC contact maps
762 for the *nhomie forward* replacement. B) MicroC contact maps for the *λDNA* replacement. C)
763 MicroC profile of the *nhomie reverse* replacement. D) MicroC profile of the *homie forward*
764 replacement.
765
766 **Fig. Supplemental 2. Expression of *CG12134* in WT (*yw*) and the four *nhomie***
767 **replacements.**
768 Digoxigenin *in situ* hybridization was used to detect expression of *CG12134* during development
769 in the indicated genetic backgrounds. Approximate developmental stages of the embryos in each
770 genetic background are shown on the right. As controls, embryos of similar stages were
771 hybridized with an *eve* probe (top to bottom: stages 5, 7, 10, 11, and 13).
772
773 **Fig. Supplemental 3. Expression of *eIF3j* (*Adam*) and *TER94* in WT (*yw*) and the four**
774 ***nhomie* replacements.** Digoxigenin *in situ* hybridization was used to detect expression of A)
775 *eIF3j* and B) *TER94* during development in the indicated genetic backgrounds. Approximate
776 developmental stages of the embryos in each genetic background are shown on right. As
777 controls embryos of a similar stages were hybridized with an *eve* probe. Note that unlike the
778 HCR-FISH results shown in Fig. 4, we can detect a low level of *eIF4j* stripe expression in WT
779 (*yw*) and *nohomie forward* St 5 embryos. The difference is likely due to the fact that the signal
780 amplification in the digoxigenin *in situ* hybridization procedure is not linear.
781
782
783 **Fig. Supplemental 4. MicroC patterns of DNA segments on left and right arm of**
784 **chromosome 2.** A) MicroC contact profiles on left arm of chromosome 2 around 3,000,000 bp.
785 Black arrow indicates that interactions between neighboring TADs are suppressed as might be
786 expected for a stem-loop configuration. The red arrow in immediately above the black arrow
787 points to contacts between next-next-(next) door neighbors that are enhanced. However, the
788 plume that is formed is one sided as indicated by the green arrow. B) MicroC contact profiles

789 for TADs on the right arm of chromosome 2. The TADs indicated by the double headed blue
790 arrow at the bottom have a complex pattern of neighborly interactions. The asterisk and purple
791 arrow indicate a potential volcano plume; however, unlike the *eve* volcano triangle and plume,
792 this plume appears to be generated by crosslinking between sequences to either side of the
793 collection of TADs indicated by the doubleheader blue arrow. The TAD-to-TAD interaction
794 patterns are further complicated by a band of enhanced crosslinking (red arrow).
795
796

797 **References**

798 Abdennur, N., and Mirny, L.A. (2020). Cooler: scalable storage for Hi-C data and other
799 genomically labeled arrays. Bioinformatics *36*, 311-316. 10.1093/bioinformatics/btz540.
800 Americo, J., Whiteley, M., Brown, J.L., Fujioka, M., Jaynes, J.B., and Kassis, J.A. (2002). A
801 complex array of DNA-binding proteins required for pairing-sensitive silencing by a polycomb
802 group response element from the Drosophila engrailed gene. Genetics *160*, 1561-1571.
803 Arzate-Mejía, R.G., Josué Cerecedo-Castillo, A., Guerrero, G., Furlan-Magaril, M., and Recillas-
804 Targa, F. (2020). In situ dissection of domain boundaries affect genome topology and gene
805 transcription in Drosophila. Nat Commun *11*, 894. 10.1038/s41467-020-14651-z.
806 Bateman, J.R., Lee, A.M., and Wu, C.T. (2006). Site-specific transformation of Drosophila via
807 phiC31 integrase-mediated cassette exchange. Genetics *173*, 769-777.
808 Batut, P.J., Bing, X.Y., Sisco, Z., Raimundo, J., Levo, M., and Levine, M.S. (2022). Genome
809 organization controls transcriptional dynamics during development. Science *375*, 566-570.
810 10.1126/science.abi7178.
811 Bell, A.C., West, A.G., and Felsenfeld, G. (2001). Insulators and boundaries: versatile regulatory
812 elements in the eukaryotic genome. Science *291*, 447-450. 10.1126/science.291.5503.447.
813 Bing, X., Ke, W., Fujioka, M., Kurbidaeva, A., Levitt, S., Levine, M., Schedl, P., and Jaynes,
814 J.B. (2023). Chromosome Structure I: Loop extrusion or boundary:boundary pairing?
815 Cai, H.N., and Shen, P. (2001). Effects of cis arrangement of chromatin insulators on enhancer-
816 blocking activity. Science *291*, 493-495.
817 Cavalheiro, G.R., Pollex, T., and Furlong, E.E. (2021). To loop or not to loop: what is the role of
818 TADs in enhancer function and gene regulation? Curr. Opin. Genet. Dev. *67*, 119-129.
819 10.1016/j.gde.2020.12.015.
820 Chen, H., Levo, M., Barinov, L., Fujioka, M., Jaynes, J.B., and Gregor, T. (2018). Dynamic
821 interplay between enhancer–promoter topology and gene activity. Nat. Genet. *50*, 1296.
822 Chetverina, D., Aoki, T., Erokhin, M., Georgiev, P., and Schedl, P. (2014). Making connections:
823 insulators organize eukaryotic chromosomes into independent cis-regulatory networks.
824 Bioessays *36*, 163-172.
825 Chetverina, D., Fujioka, M., Erokhin, M., Georgiev, P., Jaynes, J.B., and Schedl, P. (2017).
826 Boundaries of loop domains (insulators): Determinants of chromosome form and function in
827 multicellular eukaryotes. Bioessays *39*, 1600233.
828 Chetverina, D., Savitskaya, E., Maksimenko, O., Melnikova, L., Zaytseva, O., Parshikov, A.,
829 Galkin, A.V., and Georgiev, P. (2008). Red flag on the white reporter: a versatile insulator abuts
830 the white gene in Drosophila and is omnipresent in mini-white constructs. Nucleic Acids Res.
831 *36*, 929-937.
832 Choi, H.M., Calvert, C.R., Husain, N., Huss, D., Barsi, J.C., Deverman, B.E., Hunter, R.C.,
833 Kato, M., Lee, S.M., Abelin, A.C., et al. (2016). Mapping a multiplexed zoo of mRNA
834 expression. Development *143*, 3632-3637. 10.1242/dev.140137.
835 Davidson, I.F., and Peters, J.M. (2021). Genome folding through loop extrusion by SMC
836 complexes. Nat Rev Mol Cell Biol *22*, 445-464. 10.1038/s41580-021-00349-7.
837 dos Santos, G., Schroeder, A.J., Goodman, J.L., Strelets, V.B., Crosby, M.A., Thurmond, J.,
838 Emmert, D.B., Gelbart, W.M., and FlyBase, C. (2015). FlyBase: introduction of the Drosophila
839 melanogaster Release 6 reference genome assembly and large-scale migration of genome
840 annotations. Nucleic Acids Res. *43*, D690-697.
841 Erokhin, M., Gorbenko, F., Lomaev, D., Mazina, M.Y., Mikhailova, A., Garaev, A.K.,
842 Parshikov, A., Vorobyeva, N.E., Georgiev, P., Schedl, P., and Chetverina, D. (2021). Boundaries

843 potentiate polycomb response element-mediated silencing. BMC Biol. *19*, 113. 10.1186/s12915-
844 021-01047-8.
845 Fujioka, M., Emi-Sarker, Y., Yusibova, G.L., Goto, T., and Jaynes, J.B. (1999). Analysis of an
846 *even-skipped* rescue transgene reveals both composite and discrete neuronal and early
847 blastoderm enhancers, and multi-stripe positioning by gap gene repressor gradients.
848 Development *126*, 2527-2538.
849 Fujioka, M., Mistry, H., Schedl, P., and Jaynes, J.B. (2016). Determinants of Chromosome
850 Architecture: Insulator Pairing in *cis* and in *trans*. PLoS Genet. *12*, e1005889.
851 Fujioka, M., Yusibova, G.L., Zhou, J., and Jaynes, J.B. (2008). The DNA-binding Polycomb-
852 group protein Pleiohomeotic maintains both active and repressed transcriptional states through a
853 single site. Development *135*, 4131-4139.
854 Goel, V.Y., Huseyin, M.K., and Hansen, A.S. (2023). Region Capture Micro-C reveals
855 coalescence of enhancers and promoters into nested microcompartments. Nat. Genet. *55*, 1048-
856 1056. 10.1038/s41588-023-01391-1.
857 Gohl, D., Aoki, T., Blanton, J., Shanower, G., Kappes, G., and Schedl, P. (2011). Mechanism of
858 chromosomal boundary action: roadblock, sink, or loop? Genetics *187*, 731-748.
859 Gramates, L.S., Agapite, J., Attrill, H., Calvi, B.R., Crosby, M.A., Dos Santos, G., Goodman,
860 J.L., Goutte-Gattat, D., Jenkins, V.K., Kaufman, T., et al. (2022). FlyBase: a guided tour of
861 highlighted features. Genetics *220*. 10.1093/genetics/iyac035.
862 Heger, P., George, R., and Wiehe, T. (2013). Successive gain of insulator proteins in arthropod
863 evolution. Evolution *67*, 2945-2956.
864 Heger, P., and Wiehe, T. (2014). New tools in the box: an evolutionary synopsis of chromatin
865 insulators. Trends Genet. *30*, 161-171.
866 Higashi, T.L., and Uhlmann, F. (2022). SMC complexes: Lifting the lid on loop extrusion. Curr.
867 Opin. Cell Biol. *74*, 13-22. 10.1016/j.ceb.2021.12.003.
868 Hsieh, T.S., Cattoglio, C., Slobodyanyuk, E., Hansen, A.S., Rando, O.J., Tjian, R., and Darzacq,
869 X. (2020). Resolving the 3D Landscape of Transcription-Linked Mammalian Chromatin
870 Folding. Mol. Cell *78*, 539-553.e538. 10.1016/j.molcel.2020.03.002.
871 Ibragimov, A., Bing, X.Y., Shidlovskii, Y.V., Levine, M., Georgiev, P., and Schedl, P. (2023).
872 lncRNA read-through regulates the BX-C insulator Fub-1. Elife *12*. 10.7554/eLife.84711.
873 Jerković, I., Szabo, Q., Bantignies, F., and Cavalli, G. (2020). Higher-Order Chromosomal
874 Structures Mediate Genome Function. J. Mol. Biol. *432*, 676-681. 10.1016/j.jmb.2019.10.014.
875 Kassis, J.A., VanSickle, E.P., and Sensabaugh, S.M. (1991). A fragment of engrailed regulatory
876 DNA can mediate transvection of the white gene in Drosophila. Genetics *128*, 751-761.
877 Kellum, R., and Schedl, P. (1992). A group of scs elements function as domain boundaries in an
878 enhancer-blocking assay. Mol. Cell. Biol. *12*, 2424-2431.
879 Krietenstein, N., Abraham, S., Venev, S.V., Abdennur, N., Gibcus, J., Hsieh, T.S., Parsi, K.M.,
880 Yang, L., Maehr, R., Mirny, L.A., et al. (2020). Ultrastructural Details of Mammalian
881 Chromosome Architecture. Mol. Cell *78*, 554-565.e557. 10.1016/j.molcel.2020.03.003.
882 Kruse, K., Hug, C.B., and Vaquerizas, J.M. (2020). FAN-C: a feature-rich framework for the
883 analysis and visualisation of chromosome conformation capture data. Genome Biol *21*, 303.
884 10.1186/s13059-020-02215-9.
885 Kyrchanova, O., Chetverina, D., Maksimenko, O., Kullyev, A., and Georgiev, P. (2008a).
886 Orientation-dependent interaction between Drosophila insulators is a property of this class of
887 regulatory elements. Nucleic Acids Res. *36*, 7019-7028.
888 Kyrchanova, O., Ivlieva, T., Toshchakov, S., Parshikov, A., Maksimenko, O., and Georgiev, P.
889 (2011). Selective interactions of boundaries with upstream region of Abd-B promoter in

890 Drosophila bithorax complex and role of dCTCF in this process. Nucleic Acids Res. *39*, 3042-
891 3052.
892 Kyrchanova, O., Kurbidaeva, A., Sabirov, M., Postika, N., Wolle, D., Aoki, T., Maksimenko, O.,
893 Mogila, V., Schedl, P., and Georgiev, P. (2018). The bithorax complex iab-7 Polycomb response
894 element has a novel role in the functioning of the Fab-7 chromatin boundary. PLoS Genet. *14*,
895 e1007442.
896 Kyrchanova, O., Toshchakov, S., Podstreshnaya, Y., Parshikov, A., and Georgiev, P. (2008b).
897 Functional interaction between the Fab-7 and Fab-8 boundaries and the upstream promoter
898 region in the Drosophila Abd-B gene. Mol. Cell. Biol. *28*, 4188-4195.
899 Levo, M., Raimundo, J., Bing, X.Y., Sisco, Z., Batut, P.J., Ryabichko, S., Gregor, T., and
900 Levine, M.S. (2022). Transcriptional coupling of distant regulatory genes in living embryos.
901 Nature *605*, 754-760. 10.1038/s41586-022-04680-7.
902 Li, H., and Durbin, R. (2009). Fast and accurate short read alignment with Burrows-Wheeler
903 transform. Bioinformatics *25*, 1754-1760. 10.1093/bioinformatics/btp324.
904 Li, H.-B., Muller, M., Bahechar, I.A., Kyrchanova, O., Ohno, K., Georgiev, P., and Pirrotta, V.
905 (2011). Insulators, not Polycomb response elements, are required for long-range interactions
906 between Polycomb targets in Drosophila melanogaster. Mol. Cell. Biol. *31*, 616-625.
907 Little, S.C., and Gregor, T. (2018). Single mRNA Molecule Detection in Drosophila. Methods
908 Mol Biol *1649*, 127-142. 10.1007/978-1-4939-7213-5_8.
909 Matthews, N.E., and White, R. (2019). Chromatin Architecture in the Fly: Living without
910 CTCF/Cohesin Loop Extrusion?
911 Mohana, G., Dorier, J., Li, X., Mouginot, M., Smith, R.C., Malek, H., Leleu, M., Rodriguez, D.,
912 Khadka, J., Rosa, P., et al. (2023). Chromosome-level organization of the regulatory genome in
913 the Drosophila nervous system. Cell *186*, 3826-3844.e3826. 10.1016/j.cell.2023.07.008.
914 Muller, M., Hagstrom, K., Gyurkovics, H., Pirrotta, V., and Schedl, P. (1999). The mcp element
915 from the Drosophila melanogaster bithorax complex mediates long-distance regulatory
916 interactions. Genetics *153*, 1333-1356.
917 Muravyova, E., Golovnin, A., Gracheva, E., Parshikov, A., Belenkaya, T., Pirrotta, V., and
918 Georgiev, P. (2001). Loss of insulator activity by paired Su(Hw) chromatin insulators. Science
919 *291*, 495-498.
920 Perea-Resa, C., Wattendorf, L., Marzouk, S., and Blower, M.D. (2021). Cohesin: behind
921 dynamic genome topology and gene expression reprogramming. Trends Cell Biol. *31*, 760-773.
922 10.1016/j.tcb.2021.03.005.
923 Port, F., Chen, H.-M., Lee, T., and Bullock, S.L. (2014). Optimized CRISPR/Cas tools for
924 efficient germline and somatic genome engineering in Drosophila. Proceedings of the National
925 Academy of Sciences *111*, E2967-E2976.
926 Rowley, M.J., and Corces, V.G. (2018). Organizational principles of 3D genome architecture.
927 Nature Reviews Genetics *19*, 789-800.
928 Schoborg, T.A., and Labrador, M. (2010). The phylogenetic distribution of non-CTCF insulator
929 proteins is limited to insects and reveals that BEAF-32 is Drosophila lineage specific. J. Mol.
930 Evol. *70*, 74-84. 10.1007/s00239-009-9310-x.
931 Sigrist, C.J., and Pirrotta, V. (1997). Chromatin insulator elements block the silencing of a target
932 gene by the Drosophila polycomb response element (PRE) but allow trans interactions between
933 PREs on different chromosomes. Genetics *147*, 209-221.
934 Stadler, M.R., Haines, J.E., and Eisen, M.B. (2017). Convergence of topological domain
935 boundaries, insulators, and polytene interbands revealed by high-resolution mapping of
936 chromatin contacts in the early Drosophila melanogaster embryo. eLife *6*, 17.

Trcek, T., Lionnet, T., Shroff, H., and Lehmann, R. (2017). mRNA quantification using single-molecule FISH in Drosophila embryos. Nat Protoc *12*, 1326-1348. 10.1038/nprot.2017.030.
Vazquez, J., Farkas, G., Gaszner, M., Udvardy, A., Muller, M., Hagstrom, K., Gyurkovics, H., Sipos, L., Gausz, J., Galloni, M., and et al. (1993). Genetic and molecular analysis of chromatin domains. Cold Spring Harb Symp Quant Biol *58*, 45-54. 10.1101/sqb.1993.058.01.008.
Vazquez, J., Muller, M., Pirrotta, V., and Sedat, J.W. (2006). The Mcp element mediates stable long-range chromosome-chromosome interactions in Drosophila. Molecular Biology of the Cell *17*, 2158-2165.
Venken, K.J.T., Schulze, K.L., Haelterman, N.A., Pan, H., He, Y., Evans-Holm, M., Carlson, J.W., Levis, R.W., Spradling, A.C., Hoskins, R.A., and Bellen, H.J. (2011). MiMIC: a highly versatile transposon insertion resource for engineering Drosophila melanogaster genes. Nat. Methods *8*, 737-743.
Yokoshi, M., Segawa, K., and Fukaya, T. (2020). Visualizing the Role of Boundary Elements in Enhancer-Promoter Communication. Mol. Cell *78*, 224-235.e225. 10.1016/j.molcel.2020.02.007.

981
982 **FIGURES**
983
984
985

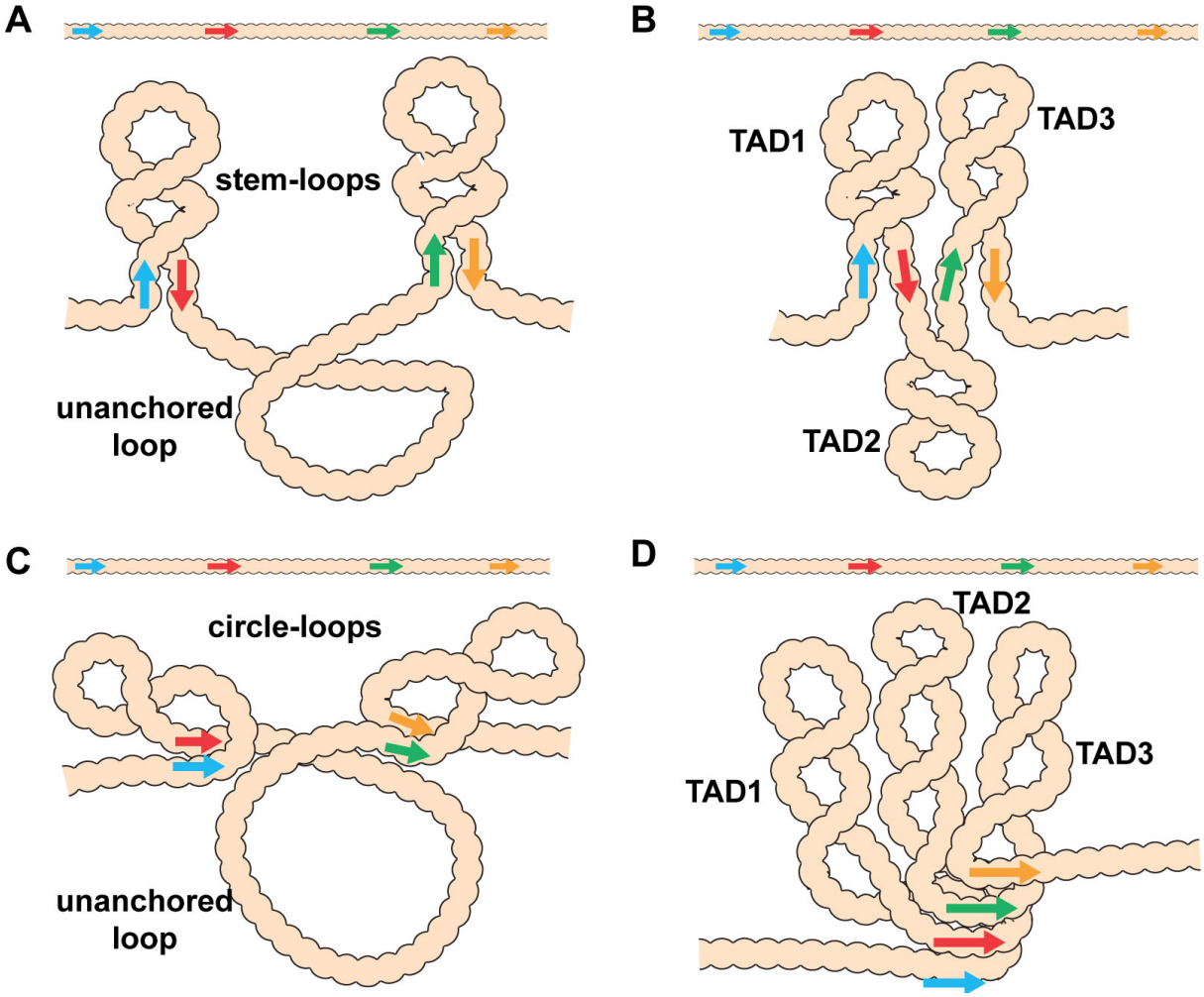

986
987 **Figure 1. Diagram of the possible loop topologies generated by head-to-head and head-to-**
988 **tail pairing.**
989
990
991

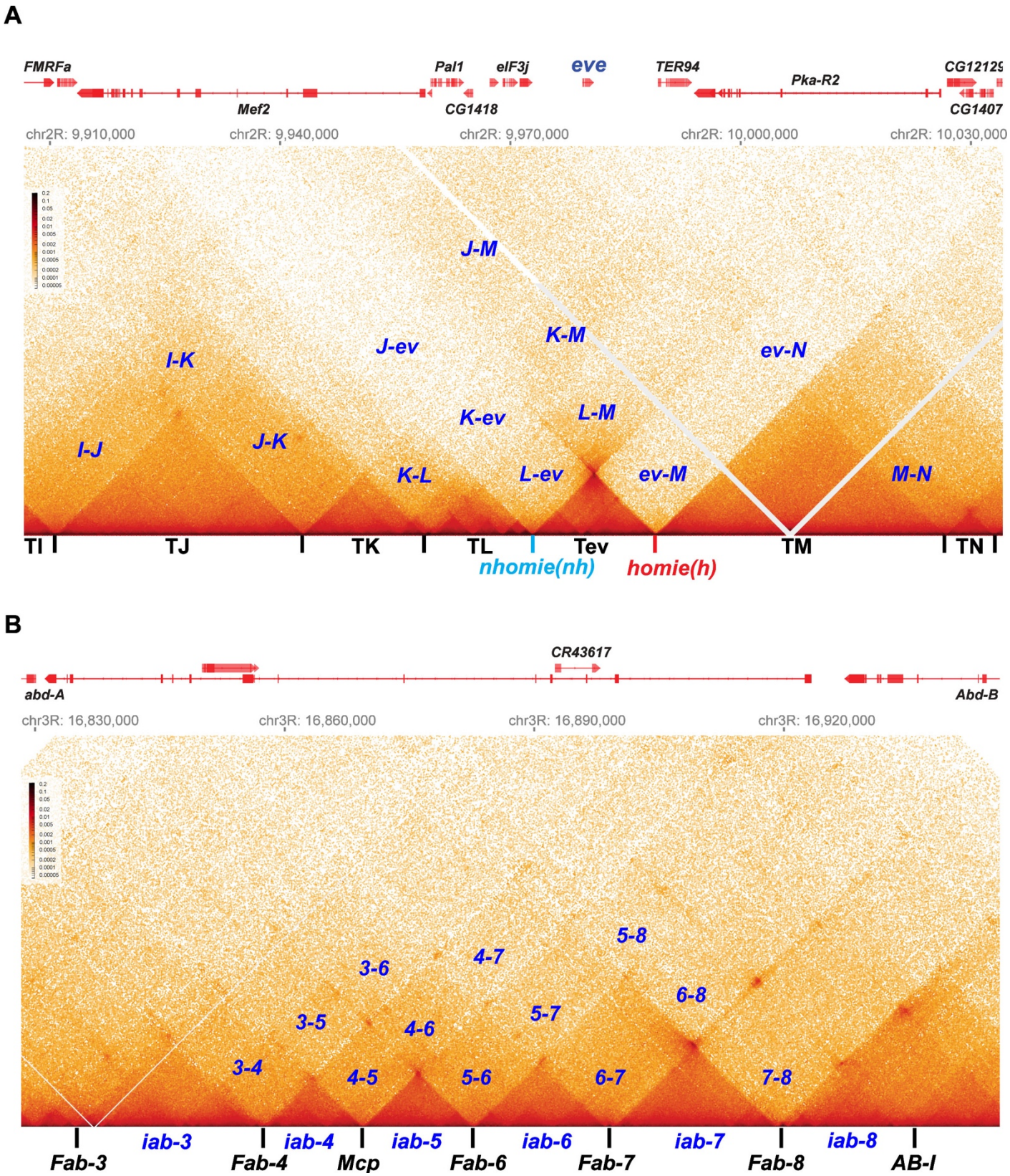

Figure 2. Stem-loops and circle-loops.

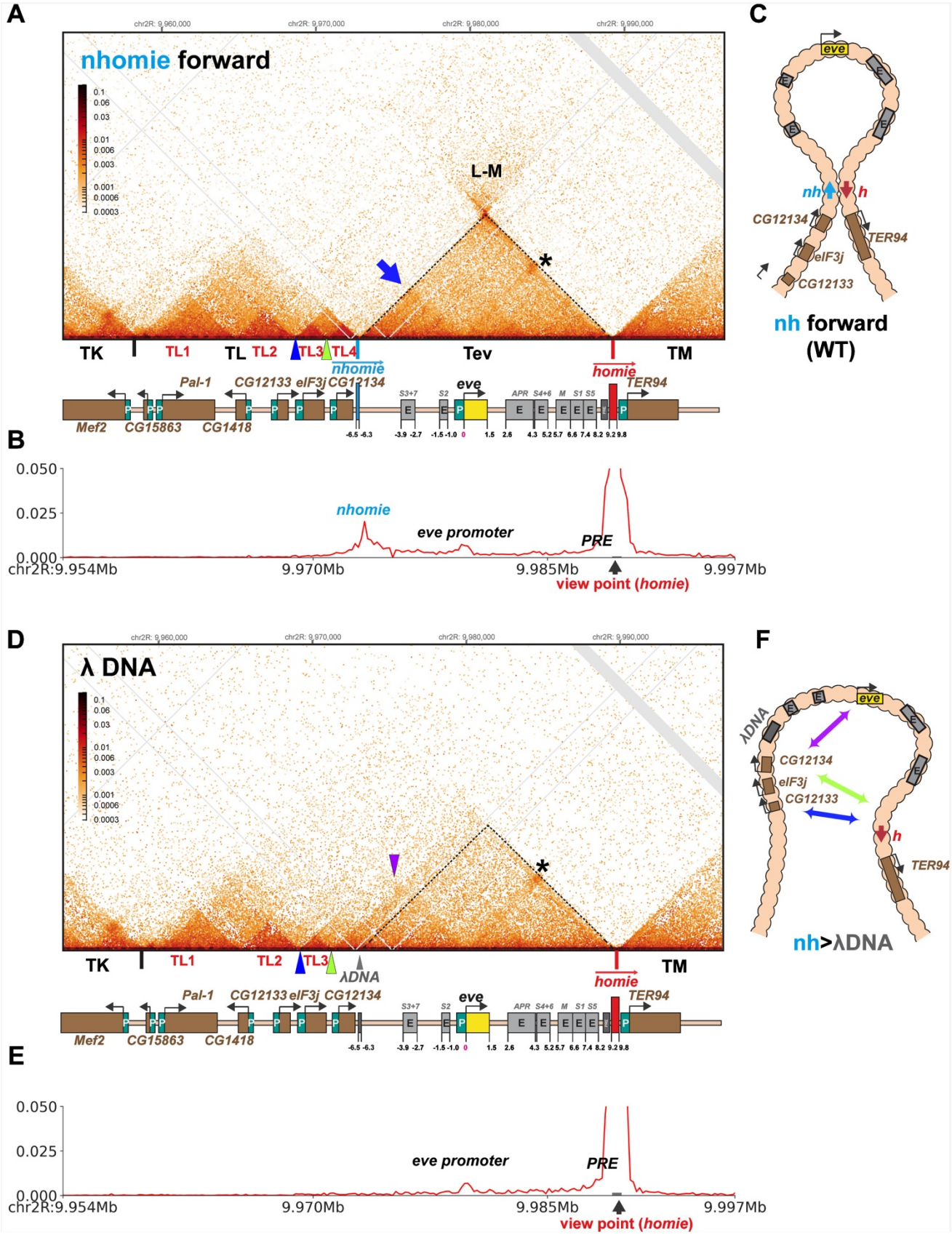

Figure 3. TAD organization of the *nhomie forward* and *λDNA* replacements.

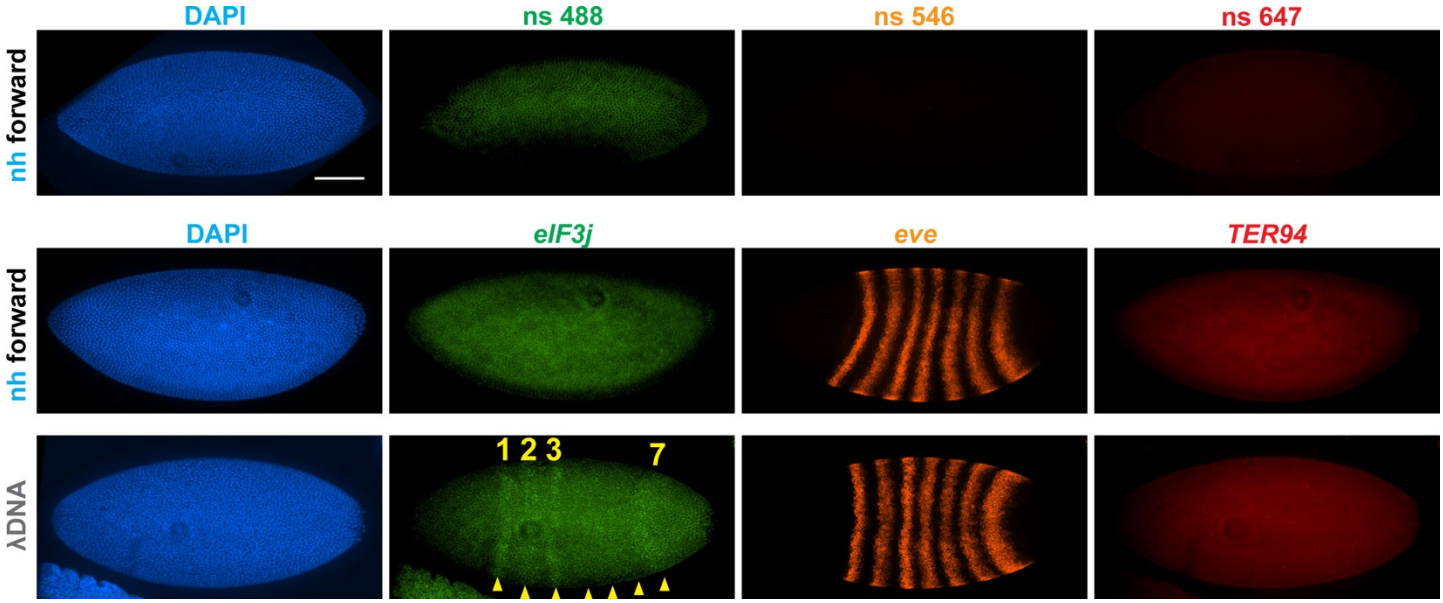

Figure 4. *nhomie* deletion (*lambda DNA* replacement) exposes *eIF3j* to the *eve* enhancers.

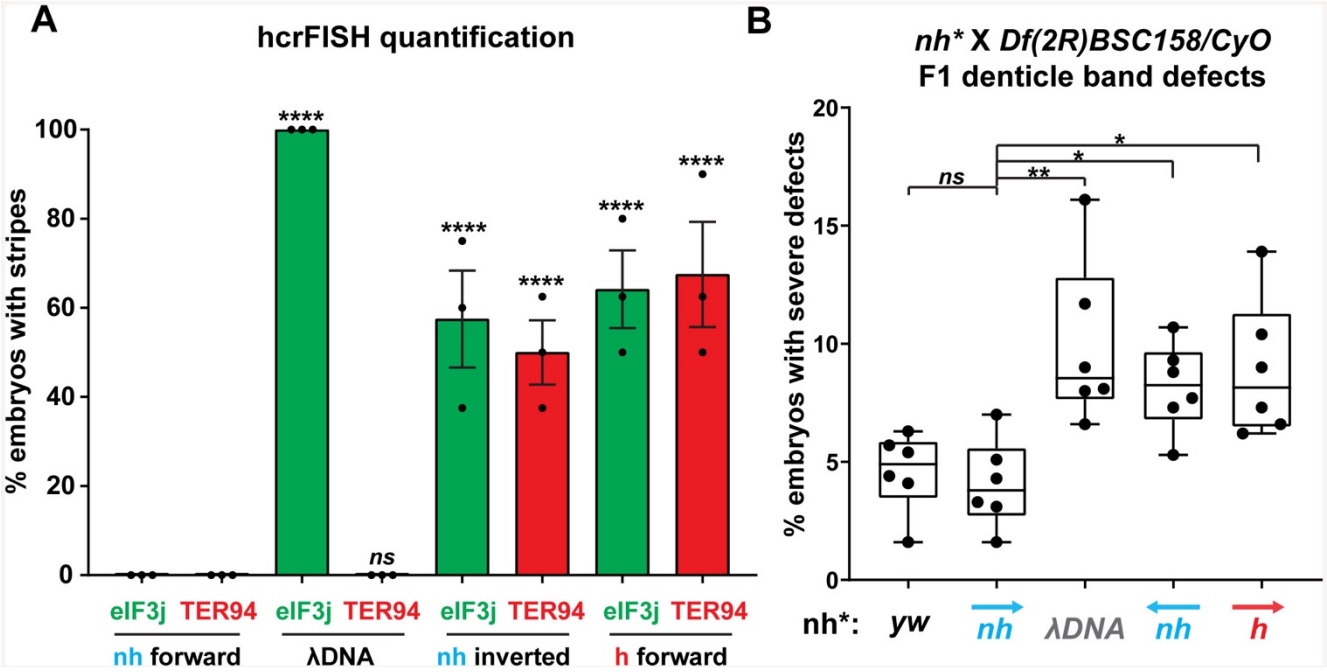

Figure 5. Manipulating the *nhomie* boundary impacts the regulatory landscape.

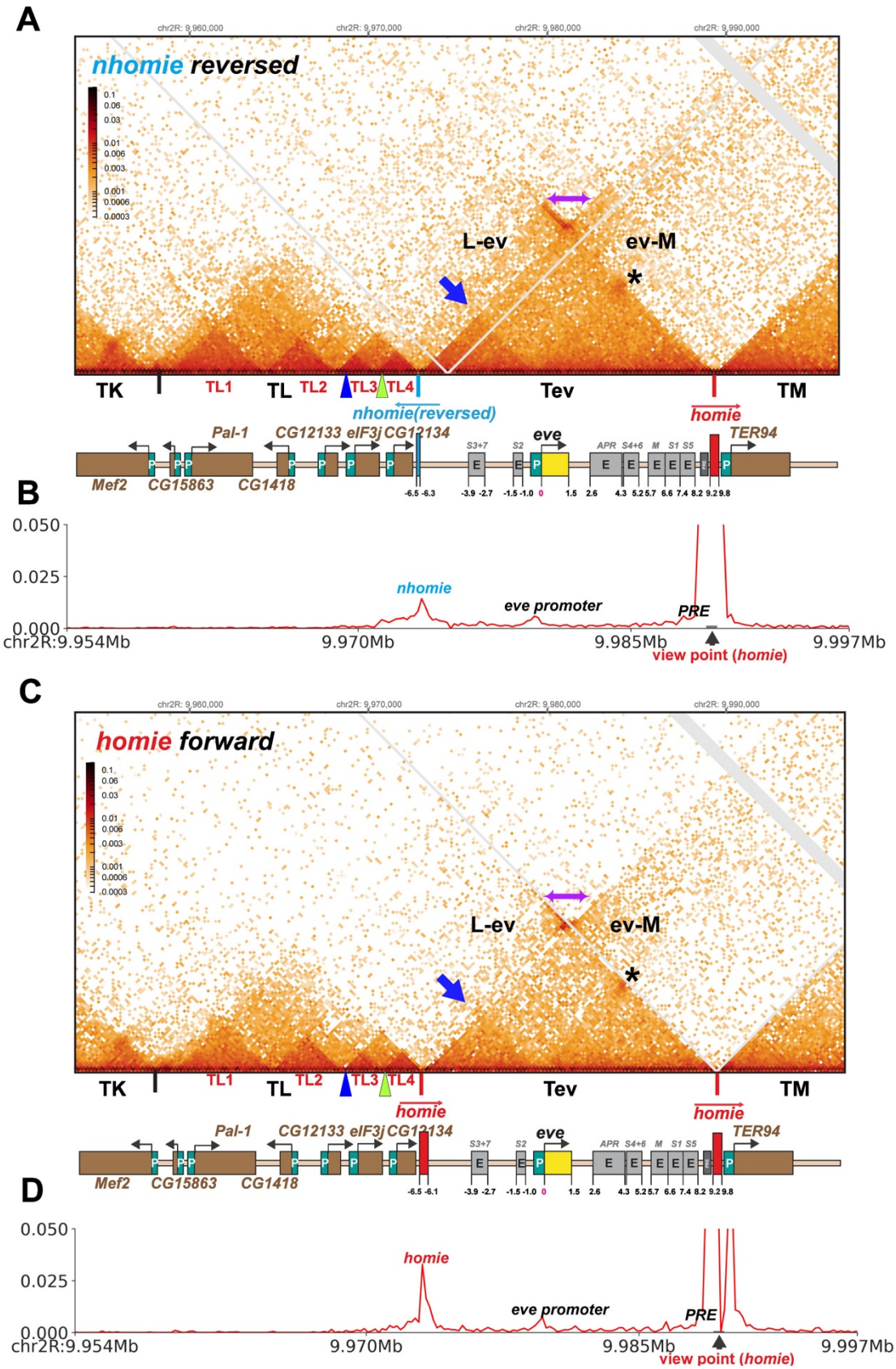

Figure 6. TAD organization of the *nhomie reverse* and *homie forward* replacements.

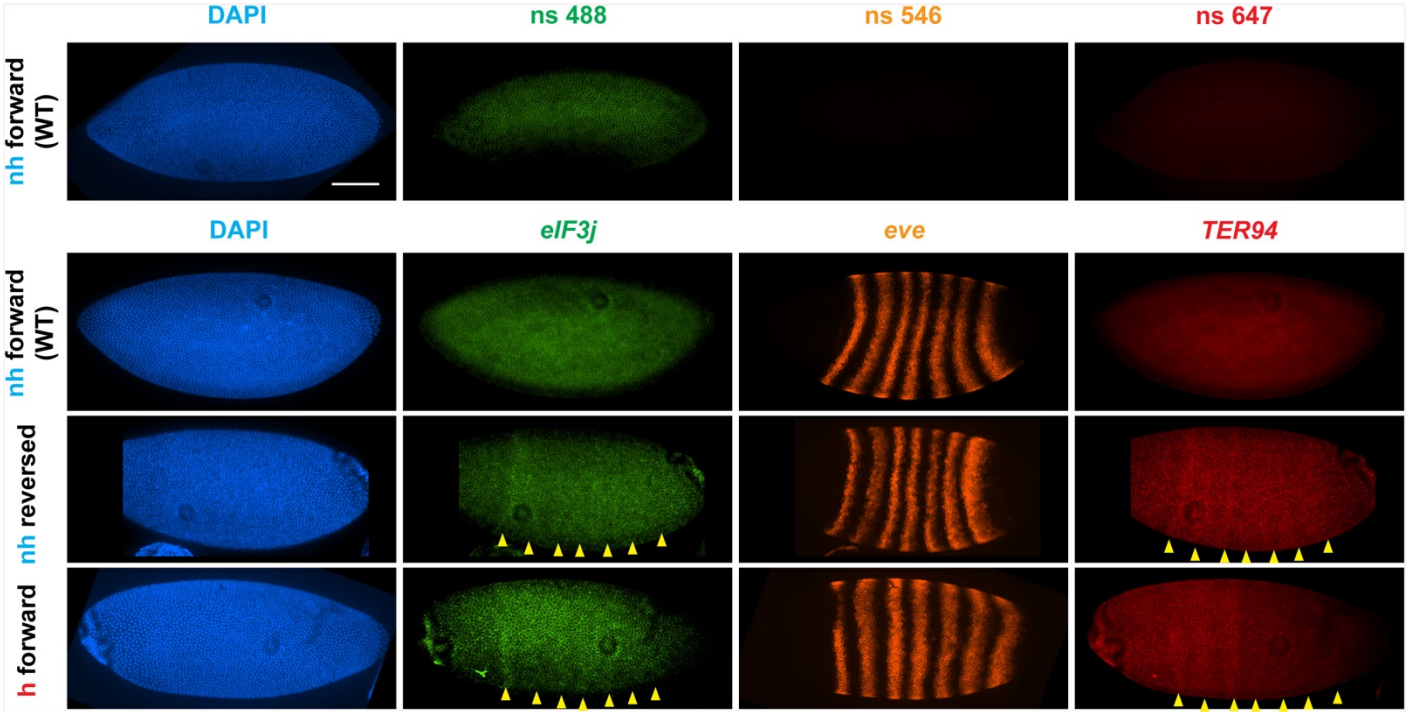

Figure 7. ***eve*** **enhancers activate neighboring genes when the** ***eve*** **TAD is a circle-loop.**